Atmos. Chem. Phys. Discuss., 13, 20341–20418, 2013
www.atmos-chem-phys-discuss.net/13/20341/2013/
doi:10.5194/acpd-13-20341-2013

Atmospheric Chemistry and Physics Discussions

Air-snowpack exchange of bromine, ozone and mercury in the springtime Arctic simulated by the 1-D model PHANTAS – Part 1: In-snow bromine activation and its impact on ozone

K. Toyota[1,2], **J. C. McConnell**[1], **R. M. Staebler**[3], **and A. P. Dastoor**[4]

[1]Department of Earth and Space Science and Engineering, York University, Toronto, Ontario, Canada
[2]Air Quality Modelling and Integration Section, Environment Canada, Toronto, Ontario, Canada
[3]Air Quality Processes Section, Environment Canada, Toronto, Ontario, Canada
[4]Air Quality Modelling and Integration Section, Environment Canada, Dorval, Quebec, Canada

Received: 9 May 2013 – Accepted: 23 July 2013 – Published: 5 August 2013

Correspondence to: K. Toyota (kenjiro.toyota@ec.gc.ca)

Published by Copernicus Publications on behalf of the European Geosciences Union.

Abstract

To provide a theoretical framework towards better understanding of ozone depletion events (ODEs) and atmospheric mercury depletion events (AMDEs) in the polar boundary layer, we have developed a one-dimensional model that simulates multiphase chemistry and transport of trace constituents from porous snowpack and through the atmospheric boundary layer (ABL) as a unified system. In this paper, we describe a general configuration of the model and the results of simulations related to reactive bromine release from the snowpack and ODEs during the Arctic spring. The model employs a chemical mechanism adapted from the one previously used for the simulation of multiphase halogen chemistry involving deliquesced sea-salt aerosols in the marine boundary layer. A common set of aqueous-phase reactions describe chemistry both in the liquid-like (or brine) layer on the grain surface of the snowpack and in "haze" aerosols mainly composed of sulfate in the atmosphere. The process of highly soluble/reactive trace gases, whether entering the snowpack from the atmosphere or formed via gas-phase chemistry in the snowpack interstitial air (SIA), is simulated by the uptake on brine-covered snow grains and subsequent reactions in the aqueous phase while being traveled vertically within the SIA.

A "bromine explosion", by which, in a conventional definition, HOBr formed in the ambient air is deposited and then converted heterogeneously to Br_2, is a dominant process of reactive bromine formation in the top 1 mm (or less) layer of the snowpack. Deeper in the snowpack, HOBr formed within the SIA leads to an in-snow bromine explosion, but a significant fraction of Br_2 is also produced via aqueous radical chemistry in the brine on the surface of the snow grains. These top- and deeper-layer productions of Br_2 both contribute to the Br_2 release into the atmosphere, but the deeper-layer production is found to be more important for the net outflux of reactive bromine. Although ozone is removed via bromine chemistry, it is also among the key species that control both the conventional and in-snow bromine explosions. On the other hand, aqueous-phase radical chemistry initiated by photolytic OH formation in the liquid-like layer is

ACPD
13, 20341–20418, 2013

also a significant contributor to the in-snow source of Br_2 and can operate without ozone, whereas the delivery of Br_2 to the atmosphere becomes much smaller after ozone is depleted. Catalytic ozone loss via bromine radicals occurs more rapidly in the SIA than in the ambient air, giving rise to apparent dry deposition velocities for ozone from the air to the snow on the order of 10^{-3} cm s^{-1} under sunlight. Overall, however, the depletion of ozone in the system is caused predominantly by ozone loss in the ambient air. Increasing depth of the turbulent ABL under windy conditions will delay the build-up of reactive bromine and the resultant loss of ozone, while leading to the higher column amount of BrO in the atmosphere. If moderately saline and acidic snowpack is as prevalent as assumed in our model runs on sea ice during the spring, the shallow, stable ABL under calm weather conditions may undergo persistent ODEs without substantial contributions from blowing/drifting snow and wind-pumping mechanisms, whereas the column densities of BrO in the ABL will likely remain too low during the course of such events to be detected unambiguously by satellite nadir measurements.

1 Introduction

Discoveries of rapid depletion events for ozone and mercury from the atmospheric boundary layer (ABL) in springtime polar regions of both hemispheres (e.g., Oltmans, 1981; Bottenheim et al., 1986; Schroeder et al., 1998; Wessel et al., 1998; Ebinghaus et al., 2002) have motivated many experimental, observational, and modeling studies to decipher key mechanisms behind this phenomenon (Simpson et al., 2007; Steffen et al., 2008; Abbatt et al., 2012, and references therein). Called ozone depletion events (ODEs) and atmospheric mercury depletion events (AMDEs), respectively, they have been observed to occur concurrently in most cases. It is now widely accepted that chain reactions involving Br atoms and BrO radicals (and IO and ClO radicals working synergistically with BrO under some circumstances) are responsible for the photochemical loss of ozone and gaseous elemental mercury during such events (Barrie et al., 1988; Hausmann and Platt, 1994; Jobson et al., 1994; Sander et al., 1997;

ACPD
13, 20341–20418, 2013

Tuckermann et al., 1997; Frieß et al., 2001; Calvert and Lindberg, 2004; Saiz-Lopez et al., 2007, 2008; Pöhler et al., 2010; Mahajan et al., 2010) in air masses that have had a recent contact with sea ice (Bottenheim et al., 1990, 2009; Hopper and Hart, 1994; Hopper et al., 1998; Frieß et al., 2004; Morin et al., 2005; Hirdman et al., 2009; Seabrook et al., 2011, 2013).

However, our understanding of how these reactive halogen species are released to the atmosphere is not well established. Various forms of salinized ice materials exist prevalently on sea ice and may react heterogeneously with atmospheric oxidants either directly as surface-bound snow/ice packs (McConnell et al., 1992; Michalowski et al., 2000; Simpson et al., 2005; Piot and von Glasow, 2008) or as wind-blown particles when windy (Rankin et al., 2002; Kaleschke et al., 2004; Yang et al., 2008; Jones et al., 2009; Frieß et al., 2011). And, if certain conditions are met, gaseous reactive halogens are released efficiently to the atmosphere. The appropriate conditions for release are not yet well established but appear to involve low temperature, sunlight and the acidity of the substrate (e.g., Fickert et al., 1999; Adams et al., 2002; Abbatt et al., 2010; Oldridge and Abbatt, 2011; Pratt et al., 2013). Our knowledge is still limited to answer clearly which of the speculated processes can indeed account for the build-up of reactive halogens and the subsequent depletion of ozone and mercury as observed under different meteorological and sea-ice phenomenological conditions (e.g., Toyota et al., 2011; Buys et al., 2013).

One suggestion on the source of reactive bromine during ODEs/AMDEs is that it is delivered mainly via a multiphase reaction sequence called “bromine explosion” (Platt and Lehrer, 1996; Wennberg, 1999; Simpson et al., 2007):

$$HOBr + Br^-_{aq} + H^+_{aq} \rightarrow Br_2 + H_2O \quad \text{(R1)}$$

$$Br_2 + h\nu \rightarrow 2\,Br \quad \text{(R2)}$$

$$Br + O_3 \rightarrow BrO + O_2 \quad \text{(R3)}$$

$$BrO + HO_2 \rightarrow HOBr + O_2 \quad \text{(R4)}$$

$$\text{net: } H^+_{aq} + Br^-_{aq} + HO_2 + O_3 \rightarrow Br + H_2O + 2\,O_2$$

ACPD
13, 20341–20418, 2013

Here, the net release of bromine from the condensed phase (e.g., snow, aerosols) to the gas phase is facilitated autocatalytically while consuming O_3 and HO_2 in the gas phase and protons in the condensed phase. Note also, the multiphase Reaction (R1) is probably an abbreviation of serial reaction steps, which, most likely, proceed via the formation of aqueous-phase intermediates $BrCl_{aq}$ and $Br_2Cl^-_{aq}$ as chloride (Cl^-) is often a few orders of magnitude more concentrated than bromide (Br^-) in polar snow on sea ice and over land near the coast (Simpson et al., 2007, and references therein). Earliest attempts to model the bromine explosion were made by box models with an ad-hoc assignment of the ventilation rate between near-surface ambient air (where HOBr is produced via R4) and saline snowpack (where HOBr is consumed to produce Br_2 via R1) (Tang and McConnell, 1996; Michalowski et al., 2000). It was implicitly assumed that the porous nature of snowpack allowed for the efficient access of ambient air throughout the bulk of the snowpack especially when ventilated by a wind-pumping process (Cunningham and Waddington, 1993). From the modeling viewpoint, this is equivalent, at least qualitatively, to placing wind-blown snow (Jones et al., 2009) and its sublimated residues (Yang et al., 2008) in the ambient air, as all the approaches will increase the effective surface area of saline snow that can interact with oxidants in the ambient air under windy conditions. On the other hand, Lehrer et al. (2004) assumed that (R1) could be represented essentially by the dry deposition of HOBr from the atmosphere onto the top of the snowpack; in their one-dimensional model of chemistry in the ABL, it took more than 20 days from the build-up of reactive bromine to the near-complete depletion of ozone. This timescale is much longer than 2–5 days as simulated by aforementioned box models in which bulk snowpack interacts with ventilated air (Tang and McConnell, 1996; Michalowski et al., 2000).

In addition to reactive bromine itself, impurities in the snowpack, especially when irradiated by sunlight, can give rise to significant emissions of short-lived chemical species including nitrogen oxides (NO, NO_2 and HONO) and aldehydes that can interact strongly with bromine chemistry in the gas phase (Grannas et al., 2007, and references therein). This, along with the abundance of ice surface available for het-

ACPD
13, 20341–20418, 2013

erogeneous reactions, will make a chemical environment in the interstitial air of the snowpack distinctly different from that in overlying ambient air. Some of these aspects were recently addressed by Thomas et al. (2011) in their one-dimensional model that described multiphase chemistry and transport processes supposedly occurring in both the snowpack and the overlying near-surface air at Summit, Greenland. With primary sources from condensed-phase photochemistry and in-snow multiphase chemical recycling such as (R1) and (R4), the model simulated the concentrations of NO and BrO in the ambient surface air in excellent agreement with in-situ field measurements, providing a strong support to chemical and physical mechanisms included in their model at least conceptually.

The purpose of this study is to explore the potential role of in-snow multiphase chemical processes in the build-up of reactive bromine and the depletion of ozone in the springtime Arctic boundary layer by developing a one-dimensional air-snowpack photochemical model similar to the one used by Thomas et al. (2011) for a study of snowpack chemistry atop the Greenland ice sheet. This paper will start from the description of physical and chemical processes included in our model, PHANTAS (a model of PHotochemistry ANd Transport between Air and Snowpack) (Sect. 2). Model simulations are then discussed with a focus on the mechanism for the release of reactive bromine and how it builds up in the snowpack and in the ABL under different meteorological conditions dictated by surface wind speeds (Sect. 3). In developing PHANTAS, great attention was given to a numerical configuration of the model for unequivocally resolving different outcomes of chemical processes in the snowpack and the overlying ambient air as well as a close connection between the two domains near the top of the snowpack by means of gas diffusion. This issue had not been addressed explicitly in most of the past modeling studies. The model framework developed here will also be used for the study of AMDEs in a companion paper (Toyota et al., 2013).

ACPD
13, 20341–20418, 2013

2 Model description

2.1 Overview

PHANTAS is a one-dimensional model that represents multiphase chemistry and vertical transport of gaseous and aqueous trace constituents through a porous snowpack and in the overlying ambient air (Fig. 1). At this point, the model is designed such that it is best suited to simulate ODEs and AMDEs in the ABL during the Arctic spring. It consists of 55 vertical grid cells, among which 22 cells represent the porous snowpack of 35 cm in depth as typically observed on Arctic sea ice in spring (Warren et al., 1999; Sturm et al., 2002) while the remaining 33 grid cells represent the turbulent ABL and extra layers in the free troposphere. The model solves a set of partial differential equations describing the temporal and vertical evolution of concentrations of the chemical species of interest:

$$\phi \frac{\partial C_g}{\partial t} = \phi \left[\frac{\partial}{\partial z} \left(D_{g,z} \frac{\partial C_g}{\partial z} \right) + P_g - L_g C_g \right] + S_g - (1-\phi) k_t \left(C_g - \frac{C_a}{K_H RT} \right) \quad (1)$$

$$\frac{\partial C_a}{\partial t} = \frac{\partial}{\partial z} \left(D_{a,z} \frac{\partial C_a}{\partial z} \right) + P_a - L_a C_a + \frac{k_t}{f_q} \left(C_g - \frac{C_a}{K_H RT} \right) \quad (2)$$

where C_g (in mole per liter of air) and C_a (in mole per liter of liquid water volume) are the concentrations of chemical species in the gas phase and in the aqueous phase, respectively, $D_{\varphi,z}$ is vertical diffusivity and P_φ and L_φ are chemical production and loss terms, respectively, in the gas phase (if $\varphi = g$) or in the aqueous phase (if $\varphi = a$), S_g is an ad-hoc source term (used here for in-snow photochemical release of HCHO and CH_3CHO), ϕ is the porosity of the snowpack or $\phi \sim 1$ in the ambient air, k_t is a mass transfer coefficient between gas- and condensed-phases (in s^{-1}), K_H is Henry's law coefficient (in $mol\,L^{-1}\,atm^{-1}$), R is gas constant ($= 0.082\,L\,atm\,mol^{-1}\,K^{-1}$), T is temperature (in Kelvin), and f_q is the volume fraction of a liquid-like layer (LLL) surrounding snow grains or $f_q = 1$ for deliquesced aerosols in the ambient air. The rate of mass

ACPD
13, 20341–20418, 2013

transfer between gas- and aqueous-phases (k_t) is calculated based on the algorithm by Schwartz (1986):

$$k_t = \left(\frac{r^2}{3D_{g,\,mol}} + \frac{4r}{3\bar{v}\alpha_m} \right)^{-1} \quad (3)$$

where r is the radius of snow grains (in the snowpack) or aerosols (in the atmosphere) for both of which monodisperse spheres are assumed, and $D_{g,\,mol}$, $\bar{v}$, and α_m are molecular diffusivity, mean thermal velocity, and mass accommodation coefficient, respectively, of a gas molecule of interest.

In the ambient air, gaseous and aerosol species are dispersed vertically by turbulent diffusion (for both gases/aerosols), molecular diffusion (for gases) or Brownian diffusion (for aerosols) depending on height and meteorological conditions (Sect. 2.7). Gas diffusion is assumed to occur further down into the snowpack interstitial air, within which the effect of wind pumping is superimposed to the molecular diffusivity in a simplified fashion (Sect. 2.4). In the snowpack, all the condensed-phase reactants and products are assumed to be contained in the LLL on the snow grains (Sect. 2.5). Also, the LLL is assumed to be connected across the entire snowpack layers, facilitating the vertical molecular diffusion of snow-trapped, aqueous-phase trace constituents although at much lower rates than would occur via gaseous molecular diffusion in the pore space (Sect. 2.6). Table 1 summarizes paramerizations adopted for calculating the vertical diffusion coefficients ($D_{g,z}$ and $D_{a,z}$) in Eqs. (1) and (2) in different model domains.

Snowpack is assumed to be made up of uniformly packed, monodisperse ice spheres with the bulk density of 0.31 g cm^{-3} as in the box model by Michalowski et al. (2000). By taking the ice mass density as 0.92 g cm^{-3}, the porosity, ϕ, is calculated to be 0.663 and the total condensed (liquid + solid) water content, $(1-\phi)/\phi$, is calculated to be 0.508 cm^3(water) cm^{-3}(air). To obtain the specific surface area (SSA) consistent with measurements for Arctic snowpack during the spring (Domine et al., 2002), the diameter of snowpack grains is adjusted to 0.3 µm, which leads to the SSA of 217 cm^2 g^{-1} of ice (or 67 cm^2 cm^{-3} of bulk space).

ACPD
13, 20341–20418, 2013

Mass continuity equations in the atmosphere, which is assumed to contain aerosols in the liquid state, are also handled by Eqs.(1)–(3) with $\phi \sim 1$ and $f_q = 1$. The liquid water content of aerosols is thus given by $(1-\phi)/\phi$. Vertical transfer of aqueous-phase species from the atmosphere to the snowpack via dry deposition of aerosols is handled by including an additional term in Eq. (2) as described in Sect. 2.8. On the other hand, no additional term is introduced for the exchange of gas-phase species between the snowpack and the atmosphere. Since compounds like O_3 (actively lost via catalytic reactions involving bromine radicals) and HOBr (taken up quickly by saline snow grains) generally maintain lower mixing ratios in the snowpack interstitial air than in the surface ambient air, "apparent" dry deposition velocities for such gases are dictated by physical and chemical processes included in the model.

2.2 Chemical mechanism

The chemical mechanism except for reactions involving mercury is adapted from Toyota et al. (2004), which was designed for simulating the multiphase chemistry of the O_x – HO_x – NO_x – VOCs($\leq C_3$) – sulfur – ClO_x – BrO_x system involving sea-salt aerosols in the marine boundary layer. New additions related to mercury chemistry are described in the companion paper (Toyota et al., 2013). Here we highlight changes from Toyota et al. (2004) in the non-mercury part of the chemical mechanism.

First, Toyota et al. (2004) accounted for the photochemistry of up to C_3 hydrocarbons and their impacts on halogen chemistry in detail (e.g., addition reactions of halogen-atoms to alkenes). Since many of these reactions were speculative on their actual occurrence but included for exploratory reasons, they are excluded in the present study except for reactions involving HCHO, CH_3CHO, and C_2H_2. Second, changes have been made in temperature dependence for the equilibrium constant between Br_2Cl^- and $BrCl(aq) + Br^-$ (Sander et al., 2006) and in the products of the aqueous-phase reaction $Br_2^- + HO_2$ from $2\,Br^- + H^+ + O_2$ to $Br_2 + HO_2^-$ (Matthew et al., 2003). Third, following the chemical mechanism developed by Herrmann et al. (2003) for the gas-aerosol-cloud system, we now assume that Br-atoms are subject to mass transfer be-

ACPD
13, 20341–20418, 2013

tween gas- and aqueous-phases. Last, absorption cross sections, quantum yields and their temperature dependence for some of the critical photolysis reactions in the aqueous phase have been updated based on recent experiments conducted on the ice surface, including the photolysis of NO_3^- for the two product channels $NO_2 + O^-$ (or OH) and $NO_2^- + O$ (Chu and Anastasio, 2003; Dubowski et al., 2002), H_2O_2 (Chu and Anastasio, 2005), NO_2^- (Chu and Anastasio, 2007), HONO and H_2ONO^+ (Anastasio and Chu, 2009). These photolytic reactions also affect halogen activation by controlling aqueous-phase OH and gas-phase NO_x concentrations in the snowpack and the overlying atmosphere.

For programming the chemical reaction component in PHANTAS, we exploited the ASAD atmospheric chemistry integration package (Carver et al., 1997), to which some adaptations have been made such as expanded arrays to deal with larger numbers of reactants and products in each aqueous-phase reaction than in gas-phase reactions and the use of the Livermore Solver for Ordinary Differential Equations with general Sparse jacobian matrix (LSODES) (Hindmarsh, 1983) for numerical integration.

2.3 Actinic flux

Actinic flux in the atmosphere is calculated with a two-stream algorithm by using the Phodis model (Kylling et al., 1995), which has been incorporated to PHANTAS for online calculations. Here we assume a clear sky on 30 March at 71° N with a total column ozone of 400 Dobson units, over the snow surface with a wavelength-independent albedo of 0.9 (Warren and Wiscombe, 1980). The actinic flux also penetrates the snowpack and is attenuated with depth in most cases. The rate of the attenuation depends most strongly on the amount of absorbing impurities such as soot, dust and organic chromophores (e.g. Warren and Wiscombe, 1980); in this work, the e-folding depth is assumed to be 7.5 cm based on direct field measurements and radiative transfer modeling for the Arctic snowpack reported previously (King and Simpson, 2001; Peterson et al., 2002; Qiu et al., 2002; Simpson et al., 2002; Reay et al., 2012). An exception to

ACPD
13, 20341–20418, 2013

this simple approximation takes place near the top of the snowpack at large solar zenith angles where significant enhancement in actinic flux can occur relative to ambient air above the snow surface (Abbatt et al., 2012). This is not addressed in the present study. Also known from field observations but neglected here is the wavelength dependence of light absorption within the snowpack which could arise from organic chromophores (King and Simpson, 2001; Beine et al., 2011).

2.4 Dispersion of trace gases in the snowpack interstitial air

Under calm weather conditions, molecular diffusion is considered to be important in controlling the exchange rate of trace gases through the snowpack interstitial air (SIA) (Albert and Shultz, 2002). To account for the mean distance over which air molecules must diffuse within the pore space of porous media, we employ an effective molecular diffusivity, $D_{g,em}$, which is a product scaled by tortuosity, τ_g, against intrinsic molecular diffusivity in free air, $D_{g,mol}$ (Bear, 1972):

$$D_{g,em} = D_{g,mol}/\tau_g. \quad (4)$$

Here, $\tau_g = 2$ is adopted to represent polar snowpack (Albert and Shultz, 2002). For gaseous species of interest in this paper (i.e., species other than mercury compounds), the values of $D_{g,mol}$ are calculated by using an empirical method by Fuller et al. (1966, 1969). The companion paper describes how $D_{g,mol}$ is calculated for mercury compounds (Toyota et al., 2013).

As wind speed increases, a form drag associated with micro-topography on the snow surface develops, leading to pressure perturbations along mean streamlines on the upwind and downwind sides of the obstacles (Cunningham and Waddington, 1993; Andreas, 1995). This also creates pressure gradients within porous snowpack and thus the ventilation of air, called "wind pumping", according to Darcy's law (Colbeck, 1989; Cunningham and Waddington, 1993; Albert, 1996). As in the previous similar model study by Thomas et al. (2011), the wind-pumping effect is superimposed as an

ACPD
13, 20341–20418, 2013

additional, effective diffusivity ($D_{g,pump}$) to the effective molecular diffusivity defined in Eq. (4), but here only where flow regime in the ambient air is diagnosed to be aerodynamically rough ($R_* > 2.5$, where R_* is the roughness Reynolds number, see Sect. 2.7), viz. at high wind speeds:

$$D_{SIA} = \begin{cases} D_{g,em} & (R_* \leq 2.5) \\ D_{g,em} + D_{g,pump} & (R_* > 2.5) \end{cases} \quad (5)$$

The total effective diffusivity (D_{SIA}) thus calculated is assumed to represent $D_{g,z}$ in Eq. (1) within the snowpack (see Table 1).

Major factors that control the wind pumping in the SIA include the micro-topographic shape of the snow surface, wind speed and direction against these structures, and permeability dictated by microphysical properties of the snowpack (Colbeck, 1989; Cunningham and Waddington, 1993). Cunningham and Waddington (1993) derived an analytical solution for the three-dimensional in-snow ventilation field of wind pumping, in which they made a number of assumptions for mathematical simplicity. Here we use the vertical component of their analytical solution after making a minor modification with regard to a boundary condition (see Appendix A):

$$D_{g,pump} = \frac{|\overline{V}_z| \times \Delta z}{\phi} \quad (6)$$

where $\overline{V}_z$, taken from Eq. (A1) in Appendix A, is an average volume flux of ventilated air and Δz is a vertical grid spacing.

2.5 Representation of liquid-like layer in snowpack

Although the nature of condensed-phase reactions in/on ice is not fully understood, the layers of disordered water molecules (called "quasi-liquid layer", or "liquid-like layer", LLL) certainly exist at the ice surface down to $T \sim 200$ K and are likely to play a critical role as a site for heterogeneous reactions (Abbatt, 2003; Domine et al., 2008). As

ACPD
13, 20341–20418, 2013

with a model study similar to ours by Thomas et al. (2011), we assume that in-snow condensed-phase reactions occur entirely within the LLL on the snow grain surface in contact with the interstitial air and that chemical species do not migrate to the solid bulk ice. Thus the volume fraction (f_q) of LLL in the total condensate relates the concentrations of aqueous-phase species in the LLL (C_a) to the bulk concentrations in the whole condensed phase (C_i) via

$$C_i = f_q C_a. \quad (7)$$

The presence of salt will significantly increase f_q (Conklin and Bales, 1993; Döppenschmidt and Butt, 2000; Voss et al., 2005) and the solute concentrations in the LLL can be estimated as a function of temperature and bulk concentrations of ionic impurities (Koop et al., 2000; Cho et al., 2002). Here we employ a simple thermodynamic equation from Cho et al. (2002) to calculate f_q at arbitrary temperature and bulk concentrations of major ions in the snow grains. Our present approach neglects the presence of brine and/or LLL that are occluded within solid ice and is thus virtually inaccessible from gases in the interstitial air (e.g., "grain boundary", see Domine et al., 2008). In this regard, the model calculates upper limits for the LLL volume involved actively in multiphase photochemical reactions within the snowpack. Errors in our estimation of the LLL volume may also arise from simplified assumptions (e.g., no precipitation of solid salts, ideal solution) in the Cho et al. equation and presently neglected (but largely unknown) contributions from various natural and anthropogenic organic compounds to the ice surface properties (e.g., Douglas et al., 2012).

2.6 Vertical diffusion of dissolved constituents in snowpack

By assuming that a majority of the LLL on the snow grains is connected between the snowpack layers, we allow for the vertical diffusion of in-snow dissolved constituents across the entire snowpack. This is equivalent to assuming that, once taken up by the ice/snow grains, trace constituents are transported via "surface diffusion" through the disordered layer on the ice surface rather than via diffusion in bulk ice (Huthwelker

ACPD
13, 20341–20418, 2013

et al., 2006; Domine et al., 2008; Gladich et al., 2011). Here, as a rough approximation, molecular diffusivity ($D_{\mathrm{aq,mol}}$) and its temperature dependence for all the constituents in the LLL are represented by the self-diffusion coefficient of supercooled water, for which we use an empirical fit to the Vogel–Fulcher–Tammann equation by Smith and Kay (1999):

$$D_{\mathrm{aq,mol}} = D_0 \exp[-E/(T - T_0)] \tag{8}$$

where $D_0 = 3.06 \times 10^{-3}\,\mathrm{cm^2\,s^{-1}}$, $E = 892\,\mathrm{K}$ and $T_0 = 118$ K. This equation gives $D_{\mathrm{aq,mol}} = 1.3 \sim 9.8 \times 10^{-6}\,\mathrm{cm^2\,s^{-1}}$ between 233–273 K. The concept of tortuosity is also applicable for estimating the effective vertical diffusivity (D_{LLL}) through the hypothetical LLL connections:

$$D_{\mathrm{LLL}} = D_{\mathrm{aq,mol}}/\tau_{\mathrm{aq}} \tag{9}$$

where the likely range of τ_{aq} for natural snow/firn is $2 \sim 3$ (Wolff and Paren, 1984; Laird et al., 1999) and here we choose $\tau_{\mathrm{aq}} = 2$ (which happens to be identical to τ_{g} while it does not have to).

2.7 Vertical diffusion in the atmospheric boundary layer

For simulating the vertical transport of trace gases and aerosols in the atmosphere, turbulent diffusivity, $K(z)$, in the stably stratified ABL is diagnosed by an empirical formula in the following form (Brost and Wyngaard, 1978):

$$K(z) = \kappa z u_* (1 - z/Z_{\mathrm{ABL}})^{1.5} \Phi_{\mathrm{H}}^{-1} \tag{10}$$

where κ is the von Kármán constant (= 0.4), z is height above the snow surface, u_* is friction velocity, Z_{ABL} is the depth of the turbulent ABL, and Φ_{H} is a stability correction term for the surface layer profile of turbulent heat transfer. Here we assume that the turbulent diffusivity is the same between heat and chemical tracers. To accommodate

ACPD
13, 20341–20418, 2013

the equation towards conditions with strong static stability, we use an expression taken from Cheng and Brutsaert (2005), rather than from Businger et al. (1971) adopted in Brost and Wyngaard (1978), for calculating Φ_H:

$$\Phi_M = 1 + a\left(\frac{\zeta + \zeta^b(1+\zeta^b)^{\frac{1-b}{b}}}{\zeta + (1+\zeta^b)^{\frac{1}{b}}}\right) \tag{11}$$

$$\Phi_H = 1 + c\left(\frac{\zeta + \zeta^d(1+\zeta^d)^{\frac{1-d}{d}}}{\zeta + (1+\zeta^d)^{\frac{1}{d}}}\right) \tag{12}$$

where $\zeta = z/L$ with L being the Obukhov length:

$$L = -\frac{\rho_{\mathrm{air}} c_p {u_*}^3 T_s}{\kappa g F_{\mathrm{SH}}} \tag{13}$$

and $a = 0.7$, $b = 0.75$, $c = 5$ and $d = 0.35$ for the stated applicability range of $0 \le \zeta \le 5$. In Eq. (13), ρ_{air} is the mass density of air, c_p is the specific heat capacity of air at constant pressure, g is acceleration due to gravity, T_s is surface air temperature (= 253 K for all the model runs, see Sect. 2.10), and F_{SH} is sensible heat flux at the surface. Φ_M is a stability correction term for momentum, used for relating wind speed (U_{ref}) at arbitrary-chosen reference height (z_{ref}) to u_* (see below). In addition to the stability functions by Cheng and Brutsaert (2005), we tested two more sets of stability functions proposed by Holtslag and de Bruin (1988) and Grachev et al. (2007), respectively. Resultant profiles of $K(z)$ from the alternative formulas were found not to be different as much as they could change general trends of model behavior discussed in this study. A major benefit of using the Cheng and Brutsaert (2005) functions, at least for our present purpose, is that numerical solutions for Eqs. (15)–(19) exist for any U_{ref} values, whereas a consistent set of U_{ref} and z_0 do not exist at low U_{ref} ($\lesssim 2\,\mathrm{m\,s^{-1}}$) when using the stability functions taken from Holtslag and de Bruin (1988) and Grachev et al. (2007).

ACPD
13, 20341–20418, 2013

For diagnosing Z_{ABL}, we use a formulation taken from Zilitinkevich and Esau (2003):

$$Z_{\mathrm{ABL}} = C_R \frac{u_*}{f}\left(1 + \frac{{C_R}^2 C_{uN}}{{C_S}^2}\frac{N}{f}\frac{{C_R}^2}{{C_S}^2}\frac{u_*}{fL}\right)^{-1/2} \tag{14}$$

where f is the Coriolis parameter and N ($= \sqrt{g/\theta \cdot \partial\theta/\partial z}$, where g is gravitational acceleration and θ is potential temperature) is the Brunt–Väisälä frequency in the free atmosphere above the turbulent ABL. Dimensionless empirical constants C_R, C_{uN} and C_S are set to 0.5, 0.56 and 1.0, respectively. The observed range of N over the Beaufort Sea during the Surface Heat Budget of the Arctic Ocean Experiment (SHEBA) was $0.016 \sim 0.046\,\mathrm{s}^{-1}$ (Steeneveld et al., 2007). Here we adopt $N = 0.031\,\mathrm{s}^{-1}$ for our model runs. The value of f is calculated for the latitude of 71° N.

We specify the profile of $K(z)$ and its diurnal variations for given U_{ref} and surface temperature (T_{s}) with prescribed sensible heat flux (F_{SH}) that varies diurnally. The calculation starts from seeking a numerical solution for u_* and z_0 that satisfy

$$\begin{aligned} U_{\mathrm{ref}} &= \int_{z_0}^{z_{\mathrm{ref}}} \frac{u_*}{\kappa z}\Phi_{\mathrm{M}}\left(\frac{z}{L}\right)\mathrm{d}z \\ &= \frac{u_*}{\kappa}\left[\ln\frac{z_{\mathrm{ref}}}{z_0} - \Psi_{\mathrm{M}}\left(\frac{z_{\mathrm{ref}}}{L}\right) + \Psi_{\mathrm{M}}\left(\frac{z_0}{L}\right)\right] \end{aligned} \tag{15}$$

where z_0 is the aerodynamic roughness length. This approach is actually inconsistent with our formulation of $K(z)$, viz. Eq. (10), in that it ignores the multiplication factor $(1 - z/Z_{\mathrm{ABL}})^{1.5}$, although it is acceptable as long as Z_{ABL} is sufficiently larger than z_{ref}. Ψ_{M} is an integral form of Φ_{M} obtained analytically (see Cheng and Brutsaert, 2005) by

$$\Psi_{\mathrm{M}}(\zeta) = \int_0^{\zeta} \frac{1 - \Phi_{\mathrm{M}}(\xi)}{\xi}\mathrm{d}\xi = -a\ln\{\zeta + [1 + \zeta^b]^{(1/b)}\}\,. \tag{16}$$

ACPD
13, 20341–20418, 2013

Similarly, Ψ_H can be obtained analytically by

$$\Psi_H(\zeta) = \int_0^{\zeta} \frac{1 - \Phi_H(\xi)}{\xi} \mathrm{d}\xi = -c \ln\{\zeta + [1 + \zeta^d]^{(1/d)}\} . \quad (17)$$

The z_0 is calculated according to Andreas et al. (2004b) by

$$z_0 = \frac{0.135\nu}{u_*} + 0.035\frac{{u_*}^2}{g}\left\{F \exp\left[-\left(\frac{u_* - 0.18}{0.1}\right)^2\right] + 1\right\} \quad (18)$$

with the empirical parameter $F = 1$ fitted to micro-meteorological data from a tower on the Beaufort Sea ice floe during the SHEBA campaign (Andreas et al., 2004a). Based on an analysis of heat flux measurements at the same meteorological tower from the SHEBA (Persson et al., 2002, see Fig. 17a), we assign a highly simplified form of diurnal variations in F_{SH} (in $\mathrm{W\,m^{-2}}$) over local solar time (LST, t) between 0–24 h:

$$F_{SH} = -5 + 4 \times \cos\left[\frac{(t - 12)\pi}{12}\right] . \quad (19)$$

This approximates the average diurnal variations in March 1998 for the SHEBA tower site.

For assigning $K(z)$ from Eq. (10) to discrete grid points in the model, we first calculate aerodynamic resistance (r_a) between the mid levels of neighboring atmospheric layers by numerically integrating the inverse of $K(z)$ over z:

$$r_{a,i} = \int_{z_{i-1}}^{z_i} K(z)^{-1} \mathrm{d}z . \quad (20)$$

ACPD
13, 20341–20418, 2013

The inverse of these $r_{a,i}$ values are then multiplied by the grid size $(z_i - z_{i-1})$ to obtain the vertical diffusivity K_i for model implementation:

$$K_i = (z_i - z_{i-1})\, {r_{a,i}}^{-1} . \quad (21)$$

In the lowest layer of the model atmosphere (1 cm thickness), we may neglect z/Z_{ABL} ($\ll 1$) in Eq. (10) so that we can integrate $1/K(z)$ analytically from the scalar roughness length (z_s) to the mid level of the layer ($z_1 = 0.5$ cm):

$$r_{a,1} = \int_{z_s}^{z_1} K(z)^{-1}\, dz \approx \frac{1}{\kappa u_*}\left[\ln\frac{z_1}{z_s} - \Psi_H\left(\frac{z_1}{L}\right) + \Psi_H\left(\frac{z_s}{L}\right)\right] . \quad (22)$$

Here, z_s changes with the ratio between kinematic viscosity (ν) of air and molecular diffusivity ($D_{g,mol}$) of trace gases (viz. Schmidt number, $Sc = \nu/D_{g,mol}$) and characteristics of turbulence dissipation in the interfacial sublayer (viz. roughness Reynolds number, $R_* = u_* z_0/\nu$) on the snow surface. Semi-empirical equations derived by Brutsaert (1975) for aerodynamically smooth ($R_* \le 0.135$) and rough ($R_* \ge 2.5$) surfaces are employed to calculate z_s:

$$z_s = \begin{cases} z_0 \exp\left[-\kappa a_v \left(13.6 Sc^{2/3} - 13.5 {a_v}^{-1}\right)\right] & (R_* \le 0.135) \\ z_0 \exp\left[-\kappa a_v \left(7.3 {R_*}^{1/4} Sc^{1/2} - 5 {a_v}^{-1}\right)\right] & (R_* \ge 2.5) \end{cases} \quad (23)$$

where ${a_v}^{-1}$ (= 1) is the turbulent Schmidt number (the ratio between eddy viscosity and eddy diffusivity) under a statically neutral condition. To fill in the gap between $0.135 \le R_* \le 2.5$, z_s/z_0 is fitted to an empirical log-log function of R_* in the same fashion as Andreas (1987):

$$\ln(z_s/z_0) = b_0 + b_1 \ln(R_*) \quad (24)$$

ACPD
13, 20341–20418, 2013

where

$$b_0 = -\kappa a_v \left(4.27 Sc^{2/3} + 6.3 Sc^{1/2} - 7.67 a_v^{-1}\right) \quad (25)$$

$$b_1 = \kappa a_v \left(4.66 Sc^{2/3} - 3.14 Sc^{1/2} - 2.91 a_v^{-1}\right). \quad (26)$$

Aerodynamic resistance as estimated above already contains a contribution from quasi-laminar layer resistance (e.g., Garratt, 1992, Chap. 3.3.3), which is usually denoted as r_b and formulated independently from r_a when calculating dry deposition velocities of trace constituents. Figure 2a and b illustrates changes in Z_{ABL} and r_a (for $HgBr_2$ at 1 m and 10 m above the snow surface), respectively, with changing reference-height wind speed (U_{ref}) and free-tropospheric Brunt–Väisälä frequency (N), calculated according to our algorithm. Since our model runs include cases where Z_{ABL} becomes lower than 10 m (but higher than 2 m), 2 m is chosen as our reference height for the surface wind speed.

The model atmosphere is divided into 33 layers with varying vertical grid size: 1 cm (first layer), 9 cm (second layer), 90 cm (third layer) and then 1 m each up to the height of 10 m above the snow surface. The remaining 21 layers above the 10 m height are evenly spaced, but the grid size is adjusted so that the top of the ABL at noon is located at the second highest model layer or below. Above Z_{ABL}, vertical diffusivity is assumed to be controlled by molecular diffusion for gases and by Brownian diffusion for aerosols. We note that the diffusivity of chemical tracers in the real atmosphere will be always and significantly greater than these theoretical lower bounds. This is because a wind shear and a breaking of internal waves act as ubiquitous sources of turbulence even above the ABL (e.g., Blackadar, 1962; Mahrt, 2011). As a preliminary test, we conducted a sensitivity study in which the vertical diffusivity of gaseous and aerosol constituents ($D_{g,z}$ and $D_{a,z}$) were both raised to arbitrary values ($10^{-4} \sim 10^{0}\ m^2\ s^{-1}$) above the height of Z_{ABL}. Its impact on simulated mixing ratios of ozone in the ABL became noticeable by using $D_{g,z} = D_{a,z} \geq 10^{-2}\ m^2\ s^{-1}$ above Z_{ABL} (not shown). Interestingly, Lagrangian models of plume chemistry and dispersion have indicated that the vertical

ACPD
13, 20341–20418, 2013

diffusivity should be in the range of $0 \sim 1\,m^2\,s^{-1}$ in the mid to upper troposphere, albeit not in the context of chemistry in the lower troposphere of the polar region (Schumann et al., 1995; Pisso et al., 2009; Real et al., 2010). This certainly implies a possibility of our model results to be affected by the diffusivity above the ABL under some circumstances, but the issue is beyond the scope of the present study.

For the derivation of $K(z)$ for each trace gas across the bottom atmospheric layer and the top snowpack layer, we add the contribution of aerodynamic resistance on the snowpack side ($= 0.5\,\Delta z / D_{SIA}$) to Eq. (22). In order to describe the rates of air–snow exchange correctly across the discrete grid points for gases (e.g., HOBr) subject to rapid heterogeneous reactions on the snow grains, the grid size of the snowpack top layer has to be sufficiently small. In this study, $\Delta z = 10^{-4}$ m is chosen for the topmost layer of snowpack and thus the extra aerodynamic resistance added to Eq. (22) is on the order of $10\,s\,m^{-1}$ for each trace gas.

2.8 Atmospheric aerosols

Heterogeneous surface reactions on atmospheric aerosols play a critical role in activating bromine chemistry by converting relatively stable HBr to photolabile Br_2 (Fan and Jacob, 1992). In the springtime Arctic, "haze" aerosols of anthropogenic origin are made up mainly of sulfate in the sub-μm size range (e.g., Quinn et al., 2007) and persistently provide the surface for such reactions to occur in the ABL. We neglect contributions from other types of aerosols, especially sea-salt aerosols, whose surface area concentrations can exceed that of the sulfate aerosols but only occasionally (Staebler et al., 1992; Yang et al., 2008). As reported in the companion paper, aerosol chemistry also influences the gas–aerosol partitioning of oxidized mercury (Toyota et al., 2013).

Hygroscopic growth of aerosols that are composed of mixed H_2SO_4-NH_4HSO_4 solution is diagnosed by the Zdanovskii–Stokes–Robinson method (Zdanovskii, 1948; Stokes and Robinson, 1966), for which experimental data for the hygroscopic growth of single-electrolyte solutions, i.e. H_2SO_4-H_2O and NH_4HSO_4-H_2O, at room tempera-

ACPD
13, 20341–20418, 2013

ture are taken from Tang and Munkelwitz (1994) and Tang (1996). For these calculations, we need to use relative humidity over liquid water, which is derived from that over ice by the Goff (1957) equation (Murphy and Koop, 2005). For example, the relative humidity of 98 % over ice (as assumed in our model runs) at 253 K and 1013.25 hPa is equivalent to the relative humidity of 80.46 % over liquid water. The density of the H_2SO_4-NH_4HSO_4-H_2O mixture, used for the calculation of dry deposition velocity, is obtained by a method described in Tang (1997).

At the beginning of each model run, aerosols are composed of 12 nmol m^{-3} (STP) of HSO_4^- and SO_4^{2-} and 9.6 nmol m^{-3} (STP) of NH_4^+, typical concentrations in the Arctic lower troposphere during spring (e.g., Fisher et al., 2011). Under the temperature and humidity conditions stated above, the initial pH of aerosols is calculated to be −0.09, in good agreement with field estimations in the Arctic boundary layer (Li, 1994; Staebler et al., 1999). The aerosols are then subject to composition changes via chemical interactions with gas-phase species and irreversible loss from the atmosphere via dry deposition to the snow surface. For this purpose, we assume monodisperse aerosols with dry diameter of 0.25 µm, which is consistent with geometric mean diameter of accumulation mode aerosols measured at Ny Ålesund in Spitsbergen during the spring of 1996 (Staebler et al., 1999). On the basis of a parameterization by Petroff and Zhang (2010), dry deposition velocities of sub-µm sulfate aerosols are calculated to be ~ 0.02 cm s^{-1} and controlled mainly by poorly characterized phoretic effects on the snow surface.

One can distribute the deposited amount of aerosol composition among the top layers of the snowpack as simulated by Cunningham and Waddington (1993). They expanded a filter collection theory, which is normally used for estimating the ability of aerosol sampling techniques, to the calculation of in-snow filtration of aerosols along the streamlines of wind-pumping flow in the interstitial air of porous snowpack. However, as noted by Harder et al. (1996), existing empirical formulas for the filtration efficiency (including the one employed by Cunningham and Waddington) only account for Brownian diffusion, impaction and interception of aerosols, but the phoretic effects (speculated as a major contributor to the dry deposition of aerosols on the snow by

ACPD
13, 20341–20418, 2013

Petroff and Zhang) are not incorporated into the formulation. Hence we choose to place the composition of deposited aerosols in the topmost layer of the snowpack as aqueous-phase species, which are then subject to vertical diffusion through (hypothetical) connections of the LLL across the snowpack layers (see Sect. 2.5). This choice also makes the numerical implementation of transport terms associated with the aerosol deposition easier, as they fit in tri-diagonal matrices employed for diffusion terms (solved by an implicit Euler method) and can thus be integrated numerically altogether in a single solver (see Sect. 2.9).

2.9 Operator splitting with a linear coupling between chemistry and transport terms

The numerical integration of our governing equations, Eqs. (1)–(3), where diffusion and chemistry are acting simultaneously, is performed by using operator splitting. But the nature of the problem addressed in this study poses a significant challenge. As mentioned in Sect. 2.7, the grid spacing at the top of the snowpack must be small enough to calculate aerodynamic resistance for gases correctly across the bottom layer of the atmosphere and the top layer of the snowpack. This constraint is most relevant to those gases which enter from the atmosphere and then interact rapidly with the snowpack LLL, as they can be completely depleted within the top layer(s) of the snowpack. For example, Br_2 is produced via reactive uptake onto the LLL of gaseous HOBr, which can either be transported via diffusion from the atmosphere or produced via gas-phase reaction (R4) in the SIA. To avoid the overshooting of HOBr from the atmosphere into the SIA while accounting for its chemical source (such as R4) and sink (such as R1) with sufficient accuracy, one may use a very short time step for the numerical integration. However, the chemical solver LSODES, which we use to handle the stiffness of differential equations for multiphase chemistry, is computationally too demanding to be executed many times at short time steps.

To solve this problem, we introduce a linear coupling between chemistry and diffusion solvers for their sequential execution via operator splitting. Its basic procedure is

ACPD
13, 20341–20418, 2013

illustrated schematically in Fig. 3. At each time step (Δt = 15 s in our model runs), the numerical integration begins with the execution of an adapted diffusion solver, which accounts for information carried over from the previous execution of an adapted chemistry solver regarding the zeroth-order chemical source term (including parameterized in-snow emissions for HCHO and CH_3CHO) and the first-order gross chemical loss rate constant, for one species after another. The loss of aerosol composition from the atmosphere via dry deposition, balanced by the input of the same constituents to the snowpack, is also taken account in the adapted diffusion solver (see below). This is followed by the execution of the adapted chemistry solver, which accounts for information carried over from the adapted diffusion solver regarding the zeroth- and first-order rates of transport-related gain and loss, for one grid cell after another. This sequence is iterated until numerical solutions for all the tracer concentrations (C_g and C_a) from the two solvers converge within given criteria, for which the relative tolerance of 10^{-3} is chosen for our model runs (but occasionally not attained as noted below).

In the adapted diffusion solver, vertical diffusion equations with linearized chemical source/sink terms are solved for gaseous and aqueous-phase species by an implicit Euler method. It employs an inversion of tri-diagonal matrices associated with diffusion and linearized chemical sink terms by LU decomposition (Press et al., 1992). As noted in Sect. 2.8, the amount of aerosol composition lost from the atmosphere via dry deposition is allocated to the LLL in the topmost grid cell of the snowpack. This represents a mass transfer between two adjacent grid cells and thus can be incorporated into the tri-diagonal matrices of the solver. Consequently, in the adapted diffusion solver, vertical mass transfer via diffusion and aerosol dry deposition, linearized effects of chemical production and loss, and in-snow emissions are taken in account simultaneously.

Since the LSODES solver (used for chemistry) employs multi-step backward differentiation formulas for representing the time differentiation of the mass continuity equations (Hindmarsh, 1983), our method of coupling between the chemistry solver and the diffusion solver (employing a single-step backward differentiation formula) risks mass conservation in the system. One manifestation of this problem is that, on about 1 % of

ACPD
13, 20341–20418, 2013

the time steps, iteration between the diffusion and chemistry solvers achieves the relative tolerance of 10^{-2} but never down to the level of 10^{-3}. Therefore, at each time step, the iteration is terminated if it is done 200 times even without achieving the desired relative tolerance of 10^{-3} (Fig. 4).

Basically, our model runs maintain non-zero vertical fluxes of gaseous and aerosol composition across the top lid of the model atmosphere by assuming molecular and Brownian diffusions for gases and aerosols, respectively, with fixed "free tropospheric" mixing ratios assumed above the top lid. By switching off these fluxes across the top lid, we tested the capability of our numerical scheme in terms of mass conservation in the system. Changes from the initial state in total bromine mass in the whole system of the atmosphere and the snowpack were found to be up to 2 % over 8 model days, whereas changes in total mercury mass approached 10 % in some model runs. Given that the present study aims at the mechanistic understanding of processes, this level of mass inconsistency is considered to be acceptable. However, this numerical aspect will need to be improved if physical and chemical processes governing the air–snowpack exchange of reactive species are to be incorporated in such a way as in our 1-D model to large-scale models for assessment purposes (e.g., impacts of atmospheric mercury deposition on the ecosystem), because mass conservation should be controlled more stringently in such models.

2.10 Simulation scenarios

One of the most important questions for halogen chemistry in the polar boundary layer is the role of temperature indicated quite often from field studies. Some studies suggested that the strong activation of bromine chemistry occurred only at temperatures around −20 °C and below (e.g., Tarasick and Bottenheim, 2002; Pöhler et al., 2010), whereas others argued that the apparent correlation between temperature and bromine activation could rather come from meteorological factors regardless of chemistry (e.g., Bottenheim et al., 2009; Jacobi et al., 2010; Toyota et al., 2011). Unfortunately, this problem cannot be addressed adequately by our model, as it presently lacks a capac-

ACPD
13, 20341–20418, 2013

ity of simulating fundamental changes in the physical properties of saline ice expected particularly below the eutectic point of hydrohalite ($NaCl \cdot 2H_2O$) at ~ 251 K (e.g., Koop et al., 2000).

Hence, in all the model runs presented in this paper, we use the same temperature, 253 K, at which saline snowpack in the polar environment likely retains properties that lead to the active release of gaseous bromine to the atmosphere (albeit with some unknowns as to why) and so does the snowpack in our model under conditions specified below. Instead, we examine the impact of changing reference-height wind speeds ($U_2 = 2, 4.5, 8.5$ and $12\,m\,s^{-1}$) on turbulent diffusivity in the near-surface atmosphere and the depth of the ABL (see Sect. 2.7), and thus the build-up rate of bromine in the atmosphere. To simplify the simulation of chemical processes, temperature, relative humidity, and pressure are all assumed to be constant with height. By neglecting changes in the relative humidity, the occurrence of cloud droplets and its consequences on halogen chemistry are also disregarded (cf. Piot and von Glasow, 2008). Table 2 summarizes meteorological and geographic conditions used in our model runs.

Table 3 gives initial conditions for condensed-phase chemistry in the snowpack. There are several ways by which the snowpack on sea ice retains seawater composition (Abbatt et al., 2012, and references therein). Here we simply take the initial concentration of Cl^- from a theoretical study by Cho et al. (2002), but it is certainly about the median level of observed concentration ranges in the uppermost layers of Arctic nearshore and coastal snowpack (e.g., Domine et al., 2004; Simpson et al., 2005). We also assume vertically uniform concentrations of dissolved in-snow constituents in the initial state of model runs. By this choice, we ignore much higher salinity often observed near the snowpack bottom on top of brine-covered, first-year sea ice (Eicken et al., 1994; Massom et al., 1998; Domine et al., 2004; Obbard et al., 2009). The initial concentration ratio between Cl^- and Br^- is set to the same as the ratio in seawater, although field observations suggest that deviation from this assumption takes place very often in the snowpack (Domine et al., 2004; Simpson et al., 2005). The initial nitrate (NO_3^-) concentration is $2\,\mu mol\,L^{-1}$, which is again about the median of observed ranges

ACPD
13, 20341–20418, 2013

in the Arctic snowpack (Grannas et al., 2007). According to the Cl^- concentration as specified above, alkalinity originally contained in seawater should be $\sim 0.3\,\mu mol\,L^{-1}$ and thus has been titrated by NO_3^-.

Bulk solutions melted from Arctic snowfall and snowpack are moderately acidic in most cases during the springtime (Gjessing, 1977; Semb et al., 1984; Toom-Sauntry and Barrie, 2002; Douglas and Sturm, 2004). Hence the value of pH in the LLL is initially set to 4; in the course of our 8 day model runs, it remains within the range of 3 ∼ 5 below the depth of 4 ∼ 9 cm (depending on model runs) in the snowpack while being lowered further towards pH ∼ 2 in the top snowpack layers primarily via dry deposition of sulfate aerosols (Fig. S1 in the Supplement). One drawback in our present simulation is that it neglects the precipitation of mirabilite ($Na_2SO_4 \cdot 10H_2O$) most likely taking place at the temperature of 253 K assumed here when sulfate aerosols enter the LLL with sufficiently high sodium content (e.g., Weeks and Hibler III, 2000, see Chap. 6). However, judging from a sensitivity study where we handled the mirabilite precipitation simply by an irreversible loss of SO_4^{2-} from the LLL, the LLL acidity is not very sensitive to this process in our simulation scenarios because a proton that has entered with the aerosols as HSO_4^- is left behind in the LLL in any case (Fig. S2 in the Supplement). In our model framework, the multiphase transfer of HCl between the SIA and the LLL also plays a critical role in buffering the pH level in the LLL. This mechanism is known to buffer the level of pH in deliquesced sea-salt aerosols across super-µm size fractions in the marine boundary layer (Keene et al., 2002). In one of the sensitivity model runs where we fixed the mixing ratios of HCl in the SIA at arbitrary values, we were able to maintain the pH level close to 4 in the LLL of the entire snowpack (Fig. S3b in the Supplement); in that case, the simulated rates of reactive bromine release from the snowpack and of concomitant ozone loss in the ABL did not change very much from those from a model run to be discussed in this paper (see Fig. S4b in the Supplement in comparison with Fig. 6b). By examining other cases in the sensitivity study with the fixed mixing ratios of HCl in the SIA, pH in the LLL was found to be an important factor for controlling the rate of reactive bromine release from the snowpack in our

ACPD
13, 20341–20418, 2013

model (Figs. S3 and S4 in the Supplement). However, to address the issue of how the pH levels evolve in the LLL of the snowpack, we should employ a more sophisticated approach than currently adopted in PHANTAS, perhaps with a deliberate treatment of processes such as the precipitation of mirabilite and other salts, the non-ideal solution behavior of a concentrated brine and the partitioning of solutes in the ice matrix (e.g., Marion and Farren, 1999; Kuo et al., 2011). This will be a subject of further studies using PHANTAS.

Table 4 lists the initial concentrations of key trace gases and aerosol composition. On the basis of the compilation of data from earlier field observations (e.g., Sander and Bottenheim, 2012), we have picked values that are deemed to be representative for air masses in the springtime Arctic lower troposphere under non-ODE conditions. These initial conditions are also used as upper boundary conditions to maintain the concentrations of trace constituents in the free troposphere under the non-ODE conditions. The initial concentrations of aerosol Br^- is set to zero in order to highlight the role of the bromine release from the snowpack. The mixing ratio of $CHBr_3$ is fixed constant at 3.5 pmol mol^{-1} in the atmosphere and the SIA. However, in contrast to a box model run by Tang and McConnell (1996), the photolysis of $CHBr_3$ makes a negligible contribution to overall bromine activation in our model runs. Among the chemical species interacting strongly with bromine in the gas phase, NO_x originates primarily from the photolysis of NO_3^- in the model snowpack. Since our chemical scheme does not have such spontaneous source mechanism for HCHO and CH_3CHO, their in-snow emissions are represented by an external source term, viz. S_g in Eq. (1), within the SIA (Table 5).

All the model runs start at 00:00 LST and are continued for 8 days with the same diurnal variations in actinic flux and vertical diffusivity. Chemical interactions of mercury with bromine and a few other reactants are also simulated in the present model runs (Toyota et al., 2013, see Sect. 2.3), but mercury species are not abundant enough to provide a notable feedback to the chemistry of bromine and ozone simulated here.

ACPD
13, 20341–20418, 2013

3 Results and discussion

3.1 Impact of changing top height and turbulent diffusivity in the ABL

Since turbulent diffusivity in the ABL is constrained by the same diurnal variations in sensible heat flux, reference-height wind speed is a primary parameter that gives changes in the vertical extent of simulated build-up of reactive bromine and resultant ozone depletion in our model runs. Figure 5 shows the profiles of vertical diffusivity in the atmosphere from models runs at $U_2 = 2\,\mathrm{m\,s^{-1}}$, $4.5\,\mathrm{m\,s^{-1}}$ and $8.5\,\mathrm{m\,s^{-1}}$, respectively. In all cases, the prescribed values of the diffusivity maximizes at local noon because of the smallest cooling rate at the surface ($F_{SH} = -1\,\mathrm{W\,m^{-2}}$), while the maximum values in the middle of the turbulent ABL change by more than an order of magnitude between the model runs. Also, the top height of the turbulent ABL changes significantly between day and night under a calm weather condition at $U_2 = 2\,\mathrm{m\,s^{-1}}$, whereas it does not at $U_2 = 4.5\,\mathrm{m\,s^{-1}}$ and $8.5\,\mathrm{m\,s^{-1}}$. Most important, noontime maximum for the top height of the ABL increases from 44 m at $U_2 = 2\,\mathrm{m\,s^{-1}}$ to 268 m at $U_2 = 8.5\,\mathrm{m\,s^{-1}}$.

As shown in Fig. 6a–c, the build-up of reactive bromine and thus the ozone depletion in the ABL takes place more swiftly as the reference-height wind speed decreases. At $U_2 = 2\,\mathrm{m\,s^{-1}}$, it takes less than 2 days to decrease the ozone mixing ratio (initially $40\,\mathrm{nmol\,mol^{-1}}$) below $20\,\mathrm{nmol\,mol^{-1}}$, whereas, at $U_2 = 4.5\,\mathrm{m\,s^{-1}}$ and $8.5\,\mathrm{m\,s^{-1}}$, it takes about 2.5 days and 3.5 days, respectively. This trend in timescale results from changes in the depth of the turbulent ABL. The shallower ABL accumulates snow-released material more rapidly. On the other hand, the decrease in the ABL depth comes with increase in aerodynamic resistance in the near-surface ambient air in our model, thereby counteracting the trend of increasing build-up rate of reactive bromine with decreasing ABL depth. As indicated from Fig. 2b, the aerodynamic resistance of ambient air to the top of snowpack is greater at $U_2 = 2\,\mathrm{m\,s^{-1}}$ by an order of magnitude (or more) than at $U_2 = 4.5\,\mathrm{m\,s^{-1}}$ and $8.5\,\mathrm{m\,s^{-1}}$. The magnitude of changes in the aerodynamic resistance thus exceeds that of the 6-fold changes in the ABL depth noted above. This appears to

ACPD
13, 20341–20418, 2013

be one of the major factors for relatively small difference in the simulated timescale for the build-up of atmospheric bromine between model runs as compared to the changes in the ABL depth.

The accumulation of snow-sourced aldehydes is another important factor. HCHO and CH_3CHO are known to have a strong potential to terminate the recycling of bromine radicals by converting Br-atom to HBr (Barrie et al., 1988; Bottenheim et al., 1990; Sander et al., 1997; Toyota et al., 2004):

$$Br + RCHO \rightarrow HCHO + RCO \quad \text{(R5)}$$

where R = H or CH_3. Several mechanisms (physical adsorption/desorption on ice surface, hydrocarbon oxidation initiated by Cl-atom, etc.) have been suggested to control the variability of aldehyde concentrations in the polar boundary layer, but the photochemical degradation of dissolved organics in the snow is definitely an important source (Grannas et al., 2007, and references therein). In our model runs, the in-snow emissions of HCHO and CH_3CHO are the predominant sources of these compounds in the entire model domain. Solid lines in Fig. 7a and b show time series in the simulated mixing ratios of HCHO and CH_3CHO and their changes with U_2 in ambient air at 1.5 m above the snowpack. At $U_2 = 2\,m\,s^{-1}$, simulated mixing ratios for HCHO and CH_3CHO in the ambient air reach over 300 pmol mol^{-1} and 200 pmol mol^{-1}, respectively, more than a factor of 2 greater than the mixing ratios for respective species at $U_2 = 4.5\,m\,s^{-1}$ and $8.5\,m\,s^{-1}$. By impeding the bromine explosion between the ambient air and the snowpack, the higher levels of aldehydes simulated at lower wind speeds not only decelerate the build-up rates of reactive bromine in the ABL (albeit not as much as overriding the faster accumulation of snow-sourced bromine in the shallower ABL, see Fig. 7c) but also raise the steady-state mixing ratios of ozone after the maturity of ODEs (Fig. 7e). At $U_2 = 2\,m\,s^{-1}$, decrease in the ozone mixing ratio stops at ~ 10 nmol mol^{-1}, whereas, at higher wind speeds, it can continue until ozone levels drop below 5 nmol mol^{-1}.

ACPD
13, 20341–20418, 2013

Simulated maxima for the atmospheric mixing ratio of HCHO shown in Fig. 7a are all within the range of field measurements in the springtime Arctic, but the mixing ratios of CH_3CHO as high as 500 pmol mol^{-1} simulated at $U_2 = 2\,m\,s^{-1}$ after ozone is depleted (see Fig. 7b) far exceed reported maxima ($\sim$ 150 pmol mol^{-1}) from field data (e.g., Grannas et al., 2002; Guimbaud et al., 2002). If those field measurements were free from instrumental artifacts and also if the data sampled a sufficiently broad range of environmental conditions, then there should be an important sink for CH_3CHO missing in our chemical scheme (e.g., Domine et al., 2010) or perhaps our choice for the in-snow emission rate of CH_3CHO may have been too high. Hence, by decreasing this ad-hoc parameter 5-fold to 8.5×10^7 molecule cm^{-2} s^{-1}, we have looked at a sensitivity of simulated results to the CH_3CHO levels (dotted lines in Fig. 7a–e). In this case, the model does not simulate higher than 100 pmol mol^{-1} for the atmospheric mixing ratio of CH_3CHO in any runs (Fig. 7b). Consequently, reactive bromine species accumulate at faster rates in the atmosphere and also reach higher levels in the course of their build up (Fig. 7c). At $U_2 = 2\,m\,s^{-1}$, the ozone mixing ratio drops from the initial level of 40 nmol mol^{-1} to lower than 10 nmol mol^{-1} in a day and half ($\sim$ 1 day shorter than in the model run with the default rate of in-snow CH_3CHO emissions). Also, the minimum mixing ratios of ozone reached on the maturity of ODEs become lower by using the lower rate of in-snow CH_3CHO emissions, as is particularly evident at $U_2 = 2\,m\,s^{-1}$ (Fig. 7e).

NO_x ($= NO + NO_2$), being supplied from the in-snow source originating from NO_3^- photolysis, is simulated to drop its mixing ratios significantly during the build-up of reactive bromine in the ABL where high BrO mixing ratios are maintained (Fig. 7c and d). This results from a formation of $BrONO_2$ followed mostly by its hydrolysis on aerosols:

$$BrO + NO_2 + M \rightarrow BrONO_2 + M \quad \text{(R6)}$$

$$BrONO_2 + H_2O_{aq} \rightarrow HOBr + HNO_3. \quad \text{(R7)}$$

Once ozone is depleted from the atmosphere, the mixing ratios of BrO drop significantly as it makes up a negligible fraction in the partitioning of inorganic bromine without an

ACPD
13, 20341–20418, 2013

adequate supply via (R3). At that point, NO_x levels in the ABL start to recover towards their new steady-state mixing ratios of about 10 to 60 pmol mol^{-1}. In model runs with the lower rate of in-snow CH_3CHO emissions at 8.5×10^7 molecule cm^{-2} s^{-1}, it is evident that NO_x being sourced from the snowpack reaches higher mixing ratios in the near-surface ambient air under less turbulent conditions at lower wind speeds. This trend is not obvious as much in model runs with the default rate of in-snow CH_3CHO emissions, because, in this case, there is a trade-off arising from a formation of peroxyacetyl nitrate ($CH_3C(O)O_2NO_2$) to scavenge NO_2 from the ABL under more stable conditions with higher CH_3CHO levels. Owing to relatively high NO_x mixing ratios simulated after the maturity of ODEs, the model run at $U_2 = 2$ m s^{-1} and with the lower rate of in-snow CH_3CHO emissions exhibits a notable recovery of ozone by its net photochemical production after reaching the minimum level of ~ 1 nmol mol^{-1} on day 3 to ~ 7 nmol mol^{-1} near the end of day 8.

To summarize the sensitivity experiments presented in this subsection, in the statically stable ABL prevalent in the springtime Arctic, the likelihood is expected to become higher at low wind speeds for air masses to experience ozone mixing ratios lower than 10 nmol mol^{-1} persistently. Surface ozone measurements at a coastal site, Barrow (71° N) in Alaska, showed the occurrence of ODEs mainly from air masses from the ice-covered ocean and locally at low wind speed conditions (Johnson et al., 2008; Helmig et al., 2012). This gives circumstantial evidence to support the correctness of our conclusion based on model simulations. On the other hand, analyses of surface ozone data obtained over the frozen Arctic Ocean highlighted the role of ozone supply from air masses not in recent contact with sea ice occurring intermittently under strong surface winds to raise otherwise very low ozone levels (e.g., Bottenheim et al., 2009; Jacobi et al., 2010). Here we stress that ozone in the near-surface air will likely be depleted more swiftly via bromine chemistry at lower wind speeds and thus under calm weather in the stable Arctic ABL. The present study confirms earlier modeling and theoretical studies with much simpler frameworks in regard to the relation between timescale to accumulate snow-sourced bromine involved in ODEs and turbulence in the

ACPD
13, 20341–20418, 2013

ABL (Lehrer et al., 2004; Jones et al., 2009). However, by using a more comprehensive modeling approach, we also find a few trade-off factors associated with correlations in turbulence strength and the depth of the ABL and with photochemical interactions between bromine, aldehydes and nitrogen oxides that are all released from snowpack with impurities. The photochemical trade-off is expected to become particularly important under the calm weather conditions, warranting continued efforts to understand what controls the behaviors of aldehydes and nitrogen oxides on the snow for a better characterization of bromine chemistry in the polar boundary layer.

3.2 Bromine explosion in the coupled atmosphere-snowpack system

As shown in Fig. 6a–c by a stark contrast in the simulated mixing ratios for BrO and Br-atom between SIA and overlying ambient air, bromine radical chemistry is substantially more active in the SIA. Thus, ozone loss occurs more rapidly in the SIA via catalytic reactions involving (R3) and (R8):

$$BrO + BrO \rightarrow 2\,Br + O_2, \qquad \text{(R8)}$$

leading to notably lower (up to $\sim 10\,\mathrm{nmol\,mol^{-1}}$) ozone mixing ratio in the SIA during sunlit hours. Figure 8a and b shows a contrast in the partitioning of bromine species between the ambient air (1.5 m above the snow) and the SIA (3.5 cm below the top of the snowpack). $BrNO_2$ and $BrONO_2$ are simulated to maintain relatively low mixing ratios ($< 2\,\mathrm{pmol\,mol^{-1}}$) and therefore omitted from these plots. In the ambient air, BrO is the most abundant bromine species during the daytime, reaching as high as $\sim 40\,\mathrm{pmol\,mol^{-1}}$ as has been measured in the field (e.g., Pöhler et al., 2010; Liao et al., 2011), until ozone mixing ratio drops below $\sim 10\,\mathrm{nmol\,mol^{-1}}$ on day 4. Before the depletion of ozone, daytime gas-phase chemistry actively produces HOBr and HBr, which are then taken up onto sulfate aerosols to give Br_2 via (R1). Br_2 is rapidly photolyzed via (R2) and thus makes an important contribution to raising the bromine radical concentrations (Fan and Jacob, 1992). In contrast, Br_2 simply accumulates at night in the ambient air and constitutes a predominant fraction among the inorganic bromine species. These

ACPD
13, 20341–20418, 2013

partitioning patterns change as ozone is depleted with time. The daytime mixing ratios of Br-atom increase with decreasing ozone mixing ratios, reaching $\sim 7\,\mathrm{pmol\,mol^{-1}}$ on days 4 and 5. This trend in the Br-atom concentrations against changes in the ozone concentrations (see also results from other runs in the third row of Fig. 6a and c) is consistent with that inferred from hydrocarbon concentration ratios in the springtime Arctic (Ramacher et al., 1999). On day 5, soon after ozone mixing ratio drops below $4\,\mathrm{nmol\,mol^{-1}}$, HBr takes over BrO as the most important bromine species in the gas phase. Also, HBr is taken up by sulfate aerosols and remains as particulate Br^- (p-Br^-) without producing Br_2. Afterwards, the nighttime build-up of Br_2 at $2 \sim 3\,\mathrm{pmol\,mol^{-1}}$ arises from its release from the snowpack.

The partitioning of gaseous bromine is vastly different in the SIA. HOBr, HBr and $BrONO_2$ are produced via gas-phase chemistry in the SIA, while they are rapidly taken up by LLL. Therefore these species never constitute major fractions in the gaseous bromine partitioning in the SIA. Under the conditions specified in our study, Br_2 is formed efficiently via the uptake of HOBr and $BrONO_2$ onto the LLL. Despite the fast photolysis of Br_2, its mixing ratio in the SIA increases sharply during the day, reaching as high as $300\,\mathrm{pmol\,mol^{-1}}$. Along with BrO formed via (R2)–(R3) and reaching $\sim 100\,\mathrm{pmol\,mol^{-1}}$ during the day, Br_2 predominates the partitioning of gaseous bromine species in the SIA. The steady-state mixing ratios of Br_2 at night in the SIA are created by a balance between the oxidation of Br^- by O_3 in the LLL (Haag and Hoigné, 1983; Oldridge and Abbatt, 2011) and the evasion of Br_2 to the atmosphere. Interestingly, even after the maturity of ODEs in the ambient air, Br_2 in the SIA builds up to mixing ratios higher than $100\,\mathrm{pmol\,mol^{-1}}$. This underlines a notable contribution to the Br_2 production from aqueous-phase radical chemistry initiated by the formation of OH via photolysis of NO_3^- and H_2O_2 in the LLL (Abbatt et al., 2010; Thomas et al., 2011). Overall, however, the "bromine explosion", viz. (R1)–(R4), is a major contributor to the build up of reactive bromine in the SIA, as indicated from higher in-snow mixing ratios of Br_2 by more than a factor of 2 before ozone is depleted at the beginning of the model run.

ACPD
13, 20341–20418, 2013

Now, what is the share of HOBr deposition from the atmosphere in the outflux of Br_2 from the snowpack? Vertical fluxes of individual bromine species across the top 1 mm of the snowpack indicate that HOBr and HBr entering from the atmosphere are both taken up almost completely within this very thin layer (Fig. 9a–c). The reactive uptake of HOBr onto LLL results in a significant addition to the Br_2 outflux within this top 1 mm layer of the snowpack. However, the net flux represented by the sum of all the gaseous bromine species does not change as much (see black dotted lines in Fig. 9a–c). As shown in Fig. 10a, the net flux of inorganic gaseous bromine accumulates over the snowpack layer, including this thin top layer but particularly within the top 5 to 10 cm. During the first couple of days, entire layers from the top of the snowpack down to ~ 25 cm depth serve as a net source of gaseous bromine, whereas, after ozone is depleted, the top 1 mm layer of the snowpack serves as a net sink of gaseous bromine for most of the time (Fig. 10b). In other words, a "bromine explosion", by which Br_2 is released from the snowpack in return for the atmospheric deposition of HOBr as set out by Lehrer et al. (2004), is a rather minor contributor to the atmospheric build-up of reactive bromine in our model. Also, the assumption that entire snowpack on sea ice is exposed to HOBr deposited from the atmosphere (Tang and McConnell, 1996; Michalowski et al., 2000) seems unrealistic even in the presence of ventilation due to wind pumping. Below the topmost layers (whose thickness is ~ 1 mm in our model), in-snow bromine activation is probably controlled by a chemical environment in the snowpack itself where ozone imported from the atmosphere and aqueous-phase radical sources (such as NO_3^-) play critical roles.

The amount of in-snow measurements from the field is not abundant enough to evaluate confidently how realistic our simulations are in terms of reactive bromine levels in the SIA. First of all, measuring the mixing ratios of reactive gases in the SIA poses a challenge, because the pumping of air for the sampling purpose can be a significant source of artifact by drawing ambient air down into the SIA (Albert et al., 2002). The only in-snow measurements that we know for gaseous reactive bromine are those performed by Foster et al. (2001) at Alert (82° N) on the next day of the first direct sunlight

ACPD
13, 20341–20418, 2013

in early March. Gaseous Br_2 mixing ratios in the top 5 cm of the snowpack were found to be enhanced to $\sim 2\,pmol\,mol^{-1}$ relative to $\sim 1\,pmol\,mol^{-1}$ in the ambient air, which does not necessarily support our results of up to $\sim 300\,pmol\,mol^{-1}$ of Br_2 simulated in the SIA. On the other hand, Peterson and Honrath (2001) reported ozone diurnal variations similar to our simulation from in-situ measurements in SIA from Summit, Greenland, during the summer. From the amplitude of daytime ozone decrease, these authors deduced higher than $160\,pmol\,mol^{-1}$ of BrO to exist in the SIA. However, such high mixing ratios of BrO were not simulated but up to about $15\,pmol\,mol^{-1}$ in the SIA by Thomas et al. (2011), who conducted a one-dimensional modeling study similar to ours to understand reactive bromine and nitrogen chemistry in the snowpack and its impacts on overlying ambient air at Summit. Neither did their simulation obtain daytime ozone decline in the SIA as large as the observation by Peterson and Honrath (2001). Recurring, large daytime declines in the in-snow ozone mixing ratios similar to Peterson and Honrath (2001) were observed later again at Summit (Helmig et al., 2007a). At Arctic coastal sites, Alert and Barrow, ozone has been found to be depleted (by more than $10\,nmol\,mol^{-1}$) persistently in SIA relative to overlying ambient air, but with no apparent diurnal variations in the mixing ratios unlike our simulations (Albert et al., 2002; Helmig et al., 2012).

We attempted a model run using the same initial condition in dissolved ion concentrations and the volume fraction of snowpack LLL as in Thomas et al. (2011), but, unfortunately, our chemical solver crashed for numerical reasons that we could not control very well before proceeding sufficient time steps to gain anything informative. One critical difference in simulated conditions between the two models is that ion concentrations in the LLL are generally more dilute in the Thomas et al. model than in ours. In part, this results from lower (initial) bulk concentrations for Cl^- and Br^- by factors of 127 and 11, respectively, used by Thomas et al. (2011) to represent the surface snow chemistry data from Summit. But, more importantly, these authors considered the LLL fraction (f_q) in the snowpack to be a turning parameter and chose $f_q = 3.3 \times 10^{-5}$, which is 3 times higher than the f_q value calculated here on the basis of a thermodynamic re-

ACPD
13, 20341–20418, 2013

lation to dissolved ion concentrations (see Table 3). Given the uncertainty in factors controlling the physics and chemistry of the LLL (see Sect. 2.5), we do not claim which of the two modeling approaches is superior to another. This is certainly one of the critical areas that need to be studied further. As discussed by Piot and von Glasow (2008) in the simulations of halogen chemistry in the polar boundary layer, cloud droplets, owing to diluted halide concentrations, are much less conducive than sea-salt aerosols to producing reactive halogens. We therefore speculate that the difference in halide concentrations between our model and the Thomas et al. model can at least partly explain rather conservative in-snow bromine activation simulated by the latter model.

3.3 Air-snow fluxes of ozone

Ozone is known to undergo dry deposition to various surfaces, including the snow surface (Helmig et al., 2007b). In essence, dry deposition velocity (v_d) at an arbitrary height can be expressed by the inverse of the sum of aerodynamic resistance (r_a), quasi-laminar layer resistance (r_b) and surface resistance (r_s):

$$v_d = (r_a + r_b + r_s)^{-1} \quad (27)$$

where r_a and r_b are determined by turbulent and molecular diffusivity in the atmosphere and r_s by solubility and reactivity on/in the substrate (Wesely, 1989). The vertical fluxes of gases (F_g) at the height where v_d is determined can then be related to their concentrations (χ_g):

$$F_g = -v_d \cdot \chi_g. \quad (28)$$

By combining the two equations above, we obtain:

$$r_s = -(\chi_g / F_g + r_a + r_b) \quad (29)$$

where χ_g, F_g and $r_a + r_b$ are all known quantities in the model. Since our model is elaborated in the parameterization of r_a and r_b (see Sect. 2.7) as well as in-snow

ACPD
13, 20341–20418, 2013

chemical processes that are linked to r_s, a comparison between the r_s values derived from the simulation by using Eq. (29) and from ozone flux measurements in the field gives a useful insight into whether or not the ozone loss simulated in our model is realistic.

Top panels in Fig. 11a–c show apparent dry deposition velocities ($v_d^* = -\chi_g/F_g$) for O_3 at four different height levels in ambient air above the snow surface as simulated at $U_2 = 2.0\,m\,s^{-1}$, $4.5\,m\,s^{-1}$ and $8.5\,m\,s^{-1}$, respectively. At the lowest height level ($z = 0.5\,cm$), the v_d^* values reach $\sim 10^{-3}\,cm\,s^{-1}$ during the day as a result of catalytic ozone loss via bromine radical chemistry, which is more active in the SIA than in the ambient air as discussed already. By simply taking an inverse of v_d^*, the minimum value of r_s for ozone on the snow surface in our model is inferred to be on the order of $10^5\,s\,m^{-1}$, as the values of r_a and r_b at $z = 0.5\,cm$ are much smaller. Interestingly, v_d^* can be more than doubled within the lowest several meters of the atmosphere, because bromine chemistry across this layer augments the downward flux of ozone from above as much as the in-snow bromine chemistry sets it out at the bottom of the atmosphere.

After the maturity of ODEs, negative dry deposition velocities for ozone become evident for model runs with $U_2 = 4.5\,m\,s^{-1}$ and $8.5\,m\,s^{-1}$. This reflects the evasion of ozone out of the SIA to the atmosphere, as the net photochemical production of ozone involving NO_x leads to higher concentrations of ozone in the SIA. However, as can be seen in Fig. 7e from changes in ozone mixing ratios in ambient air at $U_2 = 4.5\,m\,s^{-1}$ and $8.5\,m\,s^{-1}$, this in-snow source of ozone after the maturity of ODEs does not contribute much to the recovery of ozone levels in the ABL.

The reported range of r_s values for ozone on the polar snow surface is much broader than derived here from our model runs. Recently, by using ozone flux measurements at a meteorological tower, the r_s value for ozone on the snow surface at Barrow during the spring was derived to be on the order of $10^4\,s\,m^{-1}$ (Helmig et al., 2012). From a comparison of surface ozone mixing ratios simulated by a three-dimensional chemical transport model with observations across polar regions, Helmig et al. (2007a) concluded that typical dry deposition velocities on the polar snow should be on the same

ACPD
13, 20341–20418, 2013

order during the winter. Over Hudson Bay sea ice in early spring, the range of v_d^* derived from ozone flux measurements was $-1.5 \sim +0.5\,\mathrm{mm\,s^{-1}}$ (Muller et al., 2012), encompassing more an order of magnitude greater range than our simulated values. It thus seems that a sink (and a source occasionally) of ozone in the polar snow in nature is much stronger than simulated here by our model. And this again shows difficulty in proving the correctness of chemical processes that lead to in-snow bromine activation in our model.

Finally, we have plotted the v_d^* values for HOBr and HBr in the middle and bottom panels of Fig. 11a–c. As expected for compounds highly reactive on the ice surface, the high values of v_d around $1\,\mathrm{cm\,s^{-1}}$ are obtained and thus r_s is on the order of $10^2\,\mathrm{s\,m^{-1}}$. In this case, increases in v_d with height and with wind speed are both controlled essentially by changes in r_a. As noted in Sect. 3.1, this effect poses one of the important factors for modulating the build-up rate of reactive bromine in the ABL. We also stress that we had to adopt a numerical procedure of linearly-coupled iteration between the chemistry and transport solvers in order to simulate the v_d^* values correctly for these species (see Sect. 2.9).

3.4 BrO column amounts in the ABL

A major involvement of bromine radical chemistry in ODEs was first confirmed by ground-based long-path DOAS (Differential Optical Absorption Spectroscopy) measurements to detect BrO as high as $17\,\mathrm{pmol\,mol^{-1}}$ at Alert, located at the northern tip of Canada's most northerly island (Hausmann and Platt, 1994). Several years later, space-borne measurements applied the DOAS technique to spectra of sunlight reflected and/or back-scattered from the Earth and revealed a widespread occurrence of high BrO column amounts over ice-covered polar regions in both hemispheres during the spring (Chance, 1998; Richter et al., 1998; Wagner and Platt, 1998). Such measurements have been considered as unequivocal evidence to support the prevalence of high BrO levels in the springtime polar boundary layer sustained by active bromine

ACPD
13, 20341–20418, 2013

release from sea ice. Some aircraft measurements, however, indicated high BrO levels in the free troposphere as well (McElroy et al., 1999; Choi et al., 2012). Additionally, if one adopts the high end of uncertainty range in BrO levels within the upper troposphere and lower stratosphere (UTLS) region, most of the enhanced total BrO columns can be accounted for by changing partial BrO columns associated with atmospheric dynamics in the UTLS (Salawitch et al., 2010). To deal with these problems, a couple of recent studies employed stringent screening and subtraction procedures to analyze satellite BrO column data, providing more confidence in the frequent and widespread occurrence of enhanced BrO columns in the springtime polar boundary layer (Theys et al., 2011; Sihler et al., 2012).

On the other hand, while analyzing air mass origins for prolonged ODEs observed during shipboard surface ozone measurements in the middle of Arctic sea ice, Bottenheim et al. (2009) found that satellite BrO column data were not of much help to make a clear attribution of locations where the air masses may have undergone active ozone loss via bromine chemistry. A similar problem was noted from Antarctic ODEs associated with low inversion height (< 100 m) over sea ice common to low wind speed conditions (Jones et al., 2010).

The present simulations reconfirm the assertion by Jones et al. (2010). Figure 12a–d shows the simulated BrO columns in the atmosphere at $U_2 = 2$, 4.5, 8.5 and 12 m s^{-1}. Contributions from in-snow BrO columns are negligible as compared to the total column amounts in the atmosphere. Here we also include model runs with higher and lower stability (or N) assumed in the free atmosphere to investigate the problem for a broader range of the ABL depth (Z_{ABL}, see Fig. 2a). At $U_2 = 2.0$ m s^{-1} ($Z_{ABL} < 58$ m), the simulated BrO column amount does not exceed 1×10^{13} molecule cm^{-2} s^{-1}, which would hardly be discerned from variability in BrO columns above the ABL and error bars in satellite data retrieval itself. At $U_2 = 4.5$ m s^{-1} ($Z_{ABL} = 100 \sim 175$ m), BrO columns are simulated reach $1.5 \sim 2 \times 10^{13}$ molecule cm^{-2} s^{-1}, which are detectable from satellite probably with fair confidence (e.g., Theys et al., 2011). On the contrary, the maximum column amounts of BrO ($3 \sim 5 \times 10^{13}$ molecule cm^{-2} s^{-1}) simulated at

ACPD
13, 20341–20418, 2013

$U_2 = 8.5\,\mathrm{m\,s^{-1}}$ and $12\,\mathrm{m\,s^{-1}}$ ($Z_{\mathrm{ABL}} = 219 \sim 368\,\mathrm{m}$ and $352 \sim 588\,\mathrm{m}$, respectively) imply that "BrO clouds" associated with such windy events will likely be identified unambiguously from satellite unless covered under optically thick clouds. Hence, the "BrO clouds" with particularly high BrO column densities as can be seen from satellite are not necessarily a good indicator of locating the origins of ODEs (and AMDEs) observed at the ground level more often under calm weather than under stormy/gusty weather; whether or not they lead to prominent ODEs and AMDEs, such "BrO clouds" would indicate bromine activation in the deeper ABL associated with strong surface winds and/or in air masses elevated by low-pressure systems (Jones et al., 2010; Choi et al., 2012).

4 Conclusions

For a better understanding of what drives the release of reactive bromine from the snowpack over sea ice, we have developed a one-dimensional model that describes multiphase chemistry and transport of trace constituents from the porous snowpack through the atmospheric boundary layer as a unified system. The chemical mechanism has been adapted from that used for the simulation of multiphase halogen chemistry involving deliquesced sea-salt aerosols in the marine boundary layer. The formulation of vertical diffusivity and the configuration of vertical grid spacing are designed such that the model can realistically capture chemical interactions taking place between vastly different chemical environments across the interface of snowpack and overlying ambient air. The profile of turbulent diffusivity in the atmosphere is diagnosed by solving a set of micro-meteorological equations applicable to the stable boundary layer. The effect of wind pumping in the snowpack interstitial air is superimposed on molecular diffusivity in a simplified fashion and only when the surface air flow is diagnosed to be aerodynamically rough.

By elaborating both the physics and chemistry of the atmosphere-snowpack system, the present model was able to show the significance of chemical interactions that have

ACPD
13, 20341–20418, 2013

been largely unrecognized. Bromine release from the top 1 mm of the snowpack is driven by "bromine explosion" in a conventional sense, that is, HOBr deposited from the atmosphere oxidizes Br^- on the snow grains to release Br_2, whereas, below this top layer, aqueous-phase radical chemistry and in-snow "bromine explosion" both play an important role. These top- and deeper-layer processes both contribute to the Br_2 release to the atmosphere, but the deeper-layer production is generally more important for the net outflux of reactive bromine. Ozone is among the key species that control the rates of both *conventional* and *in-snow* bromine explosions. The aqueous-phase radical chemistry can keep operating as an efficient source of Br_2 in the snowpack even after ozone is depleted, but, without augmentation via the *in-snow* bromine explosion, the build-up of Br_2 and its subsequent release to the atmosphere will diminish significantly. The results of our modeling study reinforce recent findings from field measurements (Pratt et al., 2013) and from laboratory experiments (Wren et al., 2013) on the roles of snow-grain acidity and "ozone enhancement" in reactive bromine release from the snowpack. As a result of the in-snow bromine explosion, ozone is destroyed via bromine radical chemistry more actively in the SIA than in the ambient air, giving rise to apparent dry deposition velocities from the air to the snow on the order of 10^{-3} cm s^{-1} under sunlight. Field studies in attempt to determine this quantity have reported much greater values over the coastal snow cover in the springtime Arctic (Helmig et al., 2012; Muller et al., 2012), indicating either that our model is much too conservative in simulating the activity of bromine radical chemistry in the snowpack or that rapid ozone loss in/on the snow implied from those field studies was controlled by completely other mechanisms than simulated here.

In this study, the physical and chemical characteristics of the snowpack are assumed to be uniform over the entire depth in its initial state, although photochemical processing during model runs creates some degree of vertical profiles in the chemical composition of the model snowpack (e.g., the profile of Br^- residing on snow grains, see Fig. 6a–c, bottom row; see also Fig. S1 in the Supplement for the evolution of concentration profiles for major ionic components such as Cl^- and NO_3^- and of pH in the LLL). However,

ACPD
13, 20341–20418, 2013

as commonly observed in the field, the snowpack normally exhibits distinct stratigraphic features in its microphysical structure (such as coarse-grained depth hoar, hard windpack, relatively fine-grained recent snow, and surface hoar) as a result of intermittent wind storms and post-depositional metamorphosis. Such inhomogeneity in the physical properties will certainly influence chemical processes addressed in this study by changing the permeability of air against wind pumping, the rate of reactive uptake of gases on the snow grains, and so on (Domine et al., 2008). Stratigraphic variations in snowpack salinity are also common over the sea ice (Massom et al., 1998; Domine et al., 2004; Abbatt et al., 2012). From the exploratory nature of this study, we have chosen not to pursue these complex problems, but they should certainly be addressed in the future towards a more realistic representation of in-snow photochemical processes.

It has been argued that wind-blown snow over sea ice is critical to the occurrence of high BrO levels in the polar boundary layer (e.g., Yang et al., 2008; Jones et al., 2009; Frieß et al., 2011; Buys et al., 2013). However, ODEs are observed in the ABL at lower wind speeds more often than at higher wind speeds. It is possible to explain such observations by assuming blowing/drifting snow events that could have occurred back in time of the air mass history, but the present simulations indicate an efficient bromine release that can operate even without the wind-blown snow. By introducing a simplified scheme of air-snowpack chemical interaction of bromine in their three-dimension model of Arctic bromine and ozone chemistry, Toyota et al. (2011) successfully simulated the occurrence of "BrO clouds" and ODEs across the Arctic in April 2001. It was speculated that the success of the Toyota et al. (2011) model originated in its empirical parameterization by which a majority of bromine release on sea ice was associated with the dry deposition of ozone. This is qualitatively consistent with our finding in this study with detailed chemistry in the snowpack, as we also find here that in-snow chemical processes mediated by ozone provide a major part of net bromine release to the atmosphere. It is therefore important to pursue the feasibility of incorporating key processes in the snowpack physics and chemistry from this one-dimensional model into large-scale three-dimensional models albeit numerically in a much less demanding manner. As

ACPD
13, 20341–20418, 2013

surmised by Jones et al. (2009) in a highly theoretical fashion, direct bromine release from the surface snowpack could be a dominant source of bromine at low wind speeds, whereas the wind-blown snow could be far more effective as a bromine source at high wind speeds. Physical frameworks adopted (albeit quite differently to each other) in the models by Yang et al. (2008) and Jones et al. (2009) were highly elaborated in describing the blowing/drifting snow processes, but they did not come with the same level of sophistication in the description of chemistry. For a better understanding of this problem, it is worthwhile to investigate the chemistry of wind-blown snow and its link to ODEs in the polar region by using a model with a scheme of multiphase chemistry as detailed as in this study.

Appendix A

Analytical solution for wind-pumping ventilation in snowpack

With a number of assumptions to simplify mathematical treatment, Cunningham and Waddington (1993) (hereafter CW93) derived an analytical solution from governing equations for three-dimensional Darcy's flow within porous snowpack. Among others, (1) the shape of the snow surface (bumps) was assumed to follow a bi-directionally sinusoidal pattern, and (2) the microphysical properties were assumed to be uniform in the snowpack. The upper and lower boundary conditions were given by pressure perturbations associated with a form drag against surface winds over sinusoidal micro-topography at the top of the snowpack (Eq. 18 in CW93) and the absence of air ventilation across the impermeable bottom of the snowpack (Eq. 14 in CW93), respectively. However, their analytical solution did not properly account for the lower boundary condition as dictated above, but corresponded to a snowpack (or a firn) permeable to infinite depth. After reworking the analytical solution for the vertical volume flux (V_z) of ventilated air (Eq. (26) in CW93) and averaging it spatially over the horizontal domain of downward flow (which is balanced by upward flow in the remaining domain), we obtain

ACPD
13, 20341–20418, 2013

the following formula:

$$\overline{V}_z = \frac{6\,k\,\rho_{\mathrm{air}}}{\pi\,\mu\,\lambda}\frac{h}{\lambda}\frac{\sqrt{\alpha_{\mathrm{AR}}^2+1}}{\alpha_{\mathrm{AR}}}U_{10}^2 \times \left[C_1 \exp\left(-\frac{z}{\delta}\right) - C_2 \exp\left(\frac{z}{\delta}\right)\right] \quad \text{(A1)}$$

where

$$\delta = \frac{\alpha_{\mathrm{AR}}}{\sqrt{\alpha_{\mathrm{AR}}^2+1}}\frac{\lambda}{2\pi}$$

$$C_1 = \frac{\exp\left(\frac{H_{\mathrm{SD}}}{\delta}\right)}{\exp\left(\frac{H_{\mathrm{SD}}}{\delta}\right)+\exp\left(-\frac{H_{\mathrm{SD}}}{\delta}\right)}$$

$$C_2 = \frac{\exp\left(-\frac{H_{\mathrm{SD}}}{\delta}\right)}{\exp\left(\frac{H_{\mathrm{SD}}}{\delta}\right)+\exp\left(-\frac{H_{\mathrm{SD}}}{\delta}\right)}$$

and z is distance from the top of the snowpack, H_{SD} is mean snow depth (= 35 cm, Warren et al., 1999; Sturm et al., 2002), k is permeability = 4×10^{-9} m^2, Albert et al. (2002), μ is dynamic viscosity of air, U_{10} is wind speed at 10 m height (estimated from U_2), h is vertical amplitude of bumps, λ is horizontal wavelength of bumps in the direction of wind, and α_{AR} is horizontal aspect ratio of bumps so that $\alpha_{\mathrm{AR}}\lambda$ gives the wavelength of bumps perpendicular to the direction of wind.

The form drag on sea ice, as dictated by the three parameters, h, λ and α_{AR}, in the equations above, results most likely from a combination of primary roughness elements such as ridging and self-organized snowdrifts created by the action of strong winds (Andreas, 1995). The morphology of sea ice is very complex and thus remains to be characterized adequately for modeling purposes such as ours, but previous field observations of sea ice micro-topography provide a clue (e.g., Sturm et al., 2002).

ACPD
13, 20341–20418, 2013

Here we use $h = 0.15$ m, $\lambda = 10$ m and $\alpha_{AR} = 0.2$, which we consider to be realistic to represent micro-topography on the first-year sea ice under windy conditions.

Supplementary material related to this article is available online at: http://www.atmos-chem-phys-discuss.net/13/20341/2013/acpd-13-20341-2013-supplement.pdf.

Acknowledgements. This study was supported by funding from CFCAS, OME, CFI, OIT and NSERC to York University and from the Clean Air Regulatory Agenda (CARA) at Environment Canada (EC). We wish to thank L. Zhang who provided a FORTRAN program to calculate dry deposition velocities of aerosols and A. Kallaur who set up and maintained a computing environment for KT at EC.

References

Abbatt, J. P. D.: Interactions of atmospheric trace gases with ice surfaces: adsorption and reaction, Chem. Rev., 103, 4783–4800, 2003. 20352

Abbatt, J., Oldridge, N., Symington, A., Chukalovskiy, V., McWhinney, R. D., Sjostedt, S., and Cox, R. A.: Release of gas-phase halogens by photolytic generation of OH in frozen halide-nitrate solutions: an active halogen formation mechanism?, J. Phys. Chem. A, 114, 6527–6533, 2010. 20344, 20373

Abbatt, J. P. D., Thomas, J. L., Abrahamsson, K., Boxe, C., Granfors, A., Jones, A. E., King, M. D., Saiz-Lopez, A., Shepson, P. B., Sodeau, J., Toohey, D. W., Toubin, C., von Glasow, R., Wren, S. N., and Yang, X.: Halogen activation via interactions with environmental ice and snow in the polar lower troposphere and other regions, Atmos. Chem. Phys., 12, 6237–6271, doi:10.5194/acp-12-6237-2012, 2012. 20343, 20351, 20365, 20382

Adams, J. W., Holmes, N. S., and Crowley, J. N.: Uptake and reaction of HOBr on frozen and dry NaCl/NaBr surfaces between 253 and 233 K, Atmos. Chem. Phys., 2, 79–91, doi:10.5194/acp-2-79-2002, 2002. 20344

Albert, M. R.: Modeling heat, mass, and species transport in polar firn, Ann. Glaciol., 23, 138–143, 1996. 20351

Albert, M. R. and Shultz, E. F.: Snow and firn properties and air-snow transport processes at Summit, Greenland, Atmos. Environ., 36, 2789–2797, 2002. 20351
Albert, M. R., Grannas, A. M., Bottenheim, J., Shepson, P. B., and Perron, F. E.: Processes and properties of snow-air transfer in the high Arctic with application to interstitial ozone at Alert, Canada, Atmos. Environ., 36, 2779–2787, 2002. 20374, 20375, 20384
Anastasio, C. and Chu, L.: Photochemistry of nitrous acid (HONO) and nitrous acidium ion (H_2ONO^+) in aqueous solution and ice, Environ. Sci. Technol., 43, 1108–1114, 2009. 20350
Andreas, E. L.: A theory for the scalar roughness and the scalar transfer coefficients over snow and sea ice, Bound.-Lay. Meteorol., 38, 159–184, 1987. 20358
Andreas, E. L.: Air–ice drag coefficients in the western Weddell Sea 2. A model based on form drag and drifting snow, J. Geophys. Res., 100, 4833–4843, 1995. 20351, 20384
Andreas, E. L., Guest, P. S., Persson, P. O. G., Fairall, C. W., Horst, T. W., Moritz, R. E., and Semmer, S. R.: Near-surface water vapor over polar sea ice is always near ice saturation, J. Geophys. Res., 107, 8033, doi:10.1029/2000JC000411, 2002. 20403
Andreas, E. L., Jordan, R. E., Guest, P. S., Persson, P. O. G., Grachev, A. A., and Fairall, C. W.: Roughness length over snow, in: Reprints, 18th Conf. on Hydrology, 11–15 January 2004, Seattle, WA, CD-ROM, JP4.31, Amer. Meteor. Soc., 2004a. 20357
Andreas, E. L., Jordan, R. E., and Makshtas, A. P.: Simulations of snow, ice, and near-surface atmospheric processes on Ice Station Weddell, J. Hydrometeor., 5, 611–624, 2004b. 20357
Barrie, L. A., Bottenheim, J. W., Schnell, R. C., Crutzen, P. J., and Rasmussen, R. A.: Ozone destruction and photochemical reactions at polar sunrise in the lower Arctic troposphere, Nature, 334, 138–141, 1988. 20343, 20369
Bear, J.: Dynamics of Fluids in Porous Media, American Elsevier Publishing Co., New York, 1972. 20351
Beine, H., Anastasio, C., Esposito, G., Patten, K., Wilkening, E., Domine, F., Voisin, D., Barret, M., Houdier, S., and Hall, S.: Soluble, light-absorbing species in snow at Barrow, Alaska, J. Geophys. Res., 116, D00R05, doi:10.1029/2011JD016181, 2011. 20351
Blackadar, A. K.: The vertical distribution of wind and turbulent exchange in a neutral atmosphere, J. Geophys. Res., 67, 3095–3102, 1962. 20359
Bottenheim, J. W., Gallant, A. G., and Brice, K. A.: Measurements of NO_y species and O_3 at 82° N latitude, Geophys. Res. Lett., 13, 113–116, 1986. 20343

ACPD
13, 20341–20418, 2013

Bottenheim, J. W., Barrie, L. A., Atlas, E., Heidt, L. E., Niki, H., Rasmussen, R. A., and Shepson, P. B.: Depletion of lower tropospheric ozone during Arctic spring: the Polar Sunrise Experiment 1988, J. Geophys. Res., 95, 18555–18568, 1990. 20344, 20369

Bottenheim, J. W., Netcheva, S., Morin, S., and Nghiem, S. V.: Ozone in the boundary layer air over the Arctic Ocean: measurements during the TARA transpolar drift 2006–2008, Atmos. Chem. Phys., 9, 4545–4557, doi:10.5194/acp-9-4545-2009, 2009. 20344, 20364, 20371, 20379

Brost, R. A. and Wyngaard, J. C.: A model study of the stably stratified planetary boundary layer, J. Atmos. Sci., 35, 1427–1440, 1978. 20354, 20355

Brutsaert, W.: The roughness length for water vapor, sensible heat, and other scalars, J. Atmos. Sci., 32, 2028–2031, 1975. 20358

Businger, J. A., Wyngaard, J. C., Izumi, Y., and Bradley, E. F.: Flux-profile relationships in the atmospheric surface layer, J. Atmos. Sci., 28, 181–189, 1971. 20355

Buys, Z., Brough, N., Huey, L. G., Tanner, D. J., von Glasow, R., and Jones, A. E.: High temporal resolution Br_2, BrCl and BrO observations in coastal Antarctica, Atmos. Chem. Phys., 13, 1329–1343, doi:10.5194/acp-13-1329-2013, 2013. 20344, 20382

Calvert, J. G. and Lindberg, S. E.: The potential influence of iodine-containing compounds on the chemistry of the troposphere in the polar spring, II. Mercury depletion, Atmos. Environ., 38, 5105–5116, 2004. 20344

Carver, G. D., Brown, P. D., and Wild, O.: The ASAD atmospheric chemistry integration package and chemical reaction database, Comp. Phys. Comm., 105, 197–215, 1997. 20350

Chance, K.: Analysis of BrO measurements from the Global Ozone Monitoring Experiment, Geophys. Res. Lett., 25, 3335–3338, 1998. 20378

Cheng, Y. and Brutsaert, W.: Flux-profile relationships for wind speed and temperature in the stable atmospheric boundary layer, Bound.-Lay. Meteorol., 114, 519–538, 2005. 20355, 20356

Cho, H., Shepson, P. B., Barrie, L. A., Cowin, J. P., and Zaveri, R.: NMR investigation of the quasi-brine layer in ice/brine mixtures, J. Phys. Chem. B, 106, 11226–11232, 2002. 20353, 20365, 20404

Choi, S., Wang, Y., Salawitch, R. J., Canty, T., Joiner, J., Zeng, T., Kurosu, T. P., Chance, K., Richter, A., Huey, L. G., Liao, J., Neuman, J. A., Nowak, J. B., Dibb, J. E., Weinheimer, A. J., Diskin, G., Ryerson, T. B., da Silva, A., Curry, J., Kinnison, D., Tilmes, S., and Levelt, P. F.: Analysis of satellite-derived Arctic tropospheric BrO columns in conjunction with

ACPD
13, 20341–20418, 2013

aircraft measurements during ARCTAS and ARCPAC, Atmos. Chem. Phys., 12, 1255–1285, doi:10.5194/acp-12-1255-2012, 2012. 20379, 20380
Chu, L. and Anastasio, C.: Quantum yields of hydroxyl radical and nitrogen dioxide from the photolysis of nitrate on ice, J. Phys. Chem. A, 107, 9594–9602, 2003. 20350
Chu, L. and Anastasio, C.: Formation of hydroxyl radical from the photolysis of frozen hydrogen peroxide, J. Phys. Chem. A, 109, 6264–6271, 2005. 20350
Chu, L. and Anastasio, C.: Temperature and wavelength dependence of nitrite photolysis in frozen and aqueous solutions, Environ. Sci. Technol., 41, 3626–3632, 2007. 20350
Colbeck, S. C.: Air movement in snow due to windpumping, J. Glaciol., 35, 209–213, 1989. 20351, 20352
Conklin, M. H. and Bales, R. C.: SO_2 uptake on ice spheres: liquid nature of the ice–air interface, J. Geophys. Res., 98, 16851–16855, 1993. 20353
Cunningham, J. and Waddington, E. D.: Air flow and dry deposition of non-sea salt sulfate in polar firn: paleoclimatic implications, Atmos. Environ., 27, 2943–2956, 1993. 20345, 20351, 20352, 20361, 20383
Domine, F., Cabanes, A., and Legagneux, L.: Structure, microphysics, and surface area of the Arctic snowpack near Alert during the ALERT2000 campaign, Atmos. Environ., 36, 2753–2765, 2002. 20348
Domine, F., Sparapani, R., Ianniello, A., and Beine, H. J.: The origin of sea salt in snow on Arctic sea ice and in coastal regions, Atmos. Chem. Phys., 4, 2259–2271, doi:10.5194/acp-4-2259-2004, 2004. 20365, 20382
Domine, F., Albert, M., Huthwelker, T., Jacobi, H.-W., Kokhanovsky, A. A., Lehning, M., Picard, G., and Simpson, W. R.: Snow physics as relevant to snow photochemistry, Atmos. Chem. Phys., 8, 171–208, doi:10.5194/acp-8-171-2008, 2008. 20352, 20353, 20354, 20382
Domine, F., Houdier, S., Taillandier, A.-S., and Simpson, W. R.: Acetaldehyde in the Alaskan subarctic snowpack, Atmos. Chem. Phys., 10, 919–929, doi:10.5194/acp-10-919-2010, 2010. 20370
Döppenschmidt, A. and Butt, H.-J.: Measuring thickness of the liquid-like layer on ice surfaces with atomic force microscopy, Langmuir, 16, 6709–6714, 2000. 20353
Douglas, T. A. and Sturm, M.: Arctic haze, mercury and the chemical composition of snow across northwestern Alaska, Atmos. Environ., 38, 805–820, 2004. 20366
Douglas, T. A., Domine, F., Barret, M., Anastasio, C., Beine, H. J., Bottenheim, J., Grannas, A., Houdier, S., Netcheva, S., Rowland, G., Staebler, R., and Steffen, A.: Frost flowers growing in

ACPD
13, 20341–20418, 2013

the Arctic ocean–atmosphere–sea ice–snow interface: 1. chemical composition, J. Geophys. Res., 117, D00R09, doi:10.1029/2011JD016460, 2012. 20353
Dubowski, Y., Colussi, A. J., Boxe, C., and Hoffmann, M. R.: Monotonic increase of nitrite yields in the photolysis of nitrate in ice and water between 238 and 294 K, J. Phys. Chem. A, 106, 6967–6971, 2002. 20350
Ebinghaus, R., Kock, H. H., Temme, C., Einax, J. W., Lowe, A. G., Richter, A., Burrows, J. P., and Schroeder, W. H.: Antarctic springtime depletion of atmospheric mercury, Environ. Sci. Technol., 36, 1238–1244, 2002. 20343
Eicken, H., Lange, M. A., and Wadhams, P.: Characteristics and distribution patterns of snow and meteoric ice in the Weddell Sea and their contribution to the mass balance of sea ice, Ann. Geophys., 12, 80–93, doi:10.1007/s00585-994-0080-x, 1994. 20365
Evans, M. J., Jacob, D. J., Atlas, E., Cantrell, C. A., Eisele, F., Flocke, F., Fried, A., Mauldin, R. L., Ridley, B. A., Wert, B., Talbot, R., Blake, D., Heikes, B., Snow, J., Walega, J., Weinheimer, A. J., and Dibb, J.: Coupled evolution of BrO_x-ClO_x-HO_x-NO_x chemistry during bromine-catalyzed ozone depletion events in the arctic boundary layer, J. Geophys. Res., 108, 8368, doi:10.1029/2002JD002732, 2003. 20405
Fan, S.-M. and Jacob, D. J.: Surface ozone depletion in Arctic spring sustained by bromine reactions on aerosols, Nature, 359, 522–524, 1992. 20360, 20372
Fickert, S., Adams, J. W., and Crowley, J. N.: Activation of Br_2 and BrCl via uptake of HOBr onto aqueous salt solutions, J. Geophys. Res., 104, 23719–23727, 1999. 20344
Fisher, J. A., Jacob, D. J., Wang, Q., Bahreini, R., Carouge, C. C., Cubison, M. J., Dibb, J. E., Diehl, T., Jimenez, J. L., Leibensperger, E. M., Lu, Z., Meinders, M. B., Pye, H. O., Quinn, P. K., Sharma, S., Streets, D. G., van Donkelaar, A., and Yantosca, R. M.: Sources, distribution, and acidity of sulfate-ammonium aerosol in the Arctic in winter–spring, Atmos. Environ., 45, 7301–7318, 2011. 20361
Foster, K. L., Plastridge, R. A., Bottenheim, J. W., Shepson, P. B., Finlayson-Pitts, B. J., and Spicer, C. W.: The role of Br_2 and BrCl in surface ozone destruction at polar sunrise, Science, 291, 471–474, 2001. 20374
Frieß, U., Wagner, T., Pundt, I., Pfeilsticker, K., and Platt, U.: Spectroscopic measurements of tropospheric iodine oxide at Neumayer Station, Antarctica, Geophys. Res. Lett., 28, 1941–1944, 2001. 20344

ACPD
13, 20341–20418, 2013

Frieß, U., Hollwedel, J., Koönig-Langlo, G., Wagner, T., and Platt, U.: Dynamics and chemistry of tropospheric bromine explosion events in the Antarctic coastal region, J. Geophys. Res., 109, D06305, doi:10.1029/2003JD004133, 2004. 20344

Frieß, U., Sihler, H., Sander, R., Pöhler, D., Yilmaz, S., and Platt, U.: The vertical distribution of BrO and aerosols in the Arctic: measurements by active and passive differential optical absorption spectroscopy, J. Geophys. Res., 116, D00R04, doi:10.1029/2011JD015938, 2011. 20344, 20382

Fuller, E. N., Schettle, P. D., and Giddings, J. C.: A new method for prediction of binary gas-phase diffusion coefficients, Ind. Eng. Chem., 58, 19–27, 1966. 20351, 20402

Fuller, E. N., Ensley, K., and Giddings, J. C.: Diffusion of halogenated hydrocarbons in helium, effect of structure on collision cross sections, J. Phys. Chem., 73, 3679–3685, 1969. 20351, 20402

Garratt, J. R.: The Atmospheric Boundary Layer, Cambridge Univ. Press, Cambridge, UK, 1992. 20359

Gjessing, Y. T.: Episodic variations of snow contamination of an Arctic snowfield, Atmos. Environ., 11, 643–647, 1977. 20366

Gladich, I., Pfalzgraff, W., Maršálek, O., Jungwirth, P., Roselová, M., and Neshyba, S.: Arrhenius analysis of anisotropic surface self-diffusion on the prismatic facet of ice, Phys. Chem. Chem. Phys., 13, 19960–19969, 2011. 20354

Goff, J. A.: Saturation pressure of water on the new Kelvin scale, Transactions of the American Society of Heating and Air-Conditioning Engineers, 63, 347–354, 1957. 20361

Grachev, A. A., Andreas, E. L., Fairall, C. W., Guest, P. S., and Persson, P. O. G.: SHEBA flux-profile relationships in the stable atmospheric boundary layer, Bound.-Lay. Meteorol., 124, 315–333, 2007. 20355

Grannas, A. M., Shepson, P. B., Guimbaud, C., Sumner, A. L., Albert, M., Simpson, W., Dominé, F., Boudries, H., Bottenheim, J., Beine, H. J., Honrath, R., and Zhou, X.: A study of photochemical and physical processes affecting carbonyl compounds in the Arctic atmospheric boundary layer, Atmos. Environ., 36, 2733–2742, 2002. 20370, 20406

Grannas, A. M., Jones, A. E., Dibb, J., Ammann, M., Anastasio, C., Beine, H. J., Bergin, M., Bottenheim, J., Boxe, C. S., Carver, G., Chen, G., Crawford, J. H., Dominé, F., Frey, M. M., Guzmán, M. I., Heard, D. E., Helmig, D., Hoffmann, M. R., Honrath, R. E., Huey, L. G., Hutterli, M., Jacobi, H. W., Klán, P., Lefer, B., McConnell, J., Plane, J., Sander, R., Savarino, J., Shepson, P. B., Simpson, W. R., Sodeau, J. R., von Glasow, R., Weller, R., Wolff, E. W., and

ACPD
13, 20341–20418, 2013

Zhu, T.: An overview of snow photochemistry: evidence, mechanisms and impacts, Atmos. Chem. Phys., 7, 4329–4373, doi:10.5194/acp-7-4329-2007, 2007. 20345, 20366, 20369, 20404

Guimbaud, C., Grannas, A. M., Shepson, P. B., Fuentes, J. D., Boudries, H., Bottenheim, J. W., Dominé, F., Houdier, S., Perrier, S., Biesenthal, T. B., and Splawn, B. G.: Snowpack processing of acetaldehyde and acetone in the Arctic atmospheric boundary layer, Atmos. Environ., 36, 2743–2752, 2002. 20370, 20406

Haag, W. R. and Hoigné, J.: Ozonation of bromide-containing waters: kinetics of formation of hypobromous acid and bromate, Environ. Sci. Technol., 17, 261–267, 1983. 20373

Harder, S. L., Warren, S. G., Charlson, R. J., and Covert, D. S.: Filtering of air through snow as a mechanism for aerosol deposition to the Antarctic ice sheet, J. Geophys. Res., 101, 18729–18743, doi:10.1029/96JD01174, 1996. 20361

Hausmann, M. and Platt, U.: Spectroscopic measurement of bromine oxide and ozone in the high Arctic during Polar Sunrise Experiment 1992, J. Geophys. Res., 99, 25399–25413, 1994. 20343, 20378

Helmig, D., Bocquet, F., Cohen, L., and Oltmans, S. J.: Ozone uptake to the polar snowpack at Summit, Greenland, Atmos. Environ., 41, 5061–5076, 2007a. 20375, 20377

Helmig, D., Ganzeveld, L., Butler, T., and Oltmans, S. J.: The role of ozone atmosphere-snow gas exchange on polar, boundary-layer tropospheric ozone – a review and sensitivity analysis, Atmos. Chem. Phys., 7, 15–30, doi:10.5194/acp-7-15-2007, 2007b. 20376

Helmig, D., Boylan, P., Johnson, B., Oltmans, S., Fairall, C., Staebler, R., Weinheimer, A., Orlando, J., Knapp, D. J., Montzka, D. D., Flocke, F., Frieß, U., Sihler, H., and Shepson, P. B.: Ozone dynamics and snow-atmosphere exchanges during ozone depletion events at Barrow, Alaska, J. Geophys. Res., 117, D20303, doi:10.1029/2012JD017531, 2012. 20371, 20375, 20377, 20381

Herrmann, H., Majdik, Z., Ervens, B., and Weise, D.: Halogen production from aqueous tropospheric particles, Chemosphere, 52, 485–502, 2003. 20349

Hindmarsh, A. C.: ODEPACK, a systematized collection of ode solvers, in: Scientific Computing, edited by: Stepleman, R. S., Carver, M., Peskin, R., Ames, W. F., and Vichnevetsky, W. F., North-Holland, Amsterdam, 55–64, 1983. 20350, 20363

Hirdman, D., Aspmo, K., Burkhart, J. F., Eckhardt, S., Sodemann, H., and Stohl, A.: Transport of mercury in the Arctic atmosphere: evidence for a spring-time net sink and summer-time source, Geophys. Res. Lett., 36, L12814, doi:10.1029/2009GL038345, 2009. 20344

ACPD
13, 20341–20418, 2013

Holtslag, A. A. M. and de Bruin, H. A. R.: Applied modeling of the nighttime surface energy balance over land, J. Appl. Meteorol., 27, 689–704, 1988. 20355

Hopper, J. F. and Hart, W.: Meteorological aspects of the 1992 Polar Sunrise Experiment, J. Geophys. Res., 99, 25315–25328, 1994. 20344

Hopper, J. F., Barrie, L. A., Silis, A., Hart, W., Gallant, A. J., and Dryfhout, H.: Ozone and meteorology during the 1994 Polar Sunrise Experiment, J. Geophys. Res., 103, 1481–1492, 1998. 20344

Huthwelker, T., Ammann, M., and Peter, T.: The uptake of acidic gases on ice, Chem. Rev., 106, 1375–1444, 2006. 20353

Jacobi, H.-W., Morin, S., and Bottenheim, J. W.: Observation of widespread depletion of ozone in the springtime boundary layer of the central Arctic linked to mesoscale synoptic conditions, J. Geophys. Res., 115, D17302, doi:10.1029/2010JD013940, 2010. 20364, 20371

Jobson, B. T., Niki, H., Yokouchi, Y., Bottenheim, J., Hopper, F., and Leaitch, R.: Measurements of C_2-C_6 hydrocarbons during the Polar Sunrise 1992 Experiment: evidence for Cl atom and Br atom chemistry, J. Geophys. Res., 99, 25355–25368, 1994. 20343

Johnson, K. P., Blum, J. D., Keeler, G. J., and Douglas, T. A.: Investigation of the deposition and emission of mercury in arctic snow during an atmospheric mercury depletion event, J. Geophys. Res., 113, D17304, doi:10.1029/2008JD009893, 2008. 20371

Jones, A. E., Anderson, P. S., Begoin, M., Brough, N., Hutterli, M. A., Marshall, G. J., Richter, A., Roscoe, H. K., and Wolff, E. W.: BrO, blizzards, and drivers of polar tropospheric ozone depletion events, Atmos. Chem. Phys., 9, 4639–4652, doi:10.5194/acp-9-4639-2009, 2009. 20344, 20345, 20372, 20382, 20383

Jones, A. E., Anderson, P. S., Wolff, E. W., Roscoe, H. K., Marshall, G. J., Richter, A., Brough, N., and Colwell, S. R.: Vertical structure of Antarctic tropospheric ozone depletion events: characteristics and broader implications, Atmos. Chem. Phys., 10, 7775–7794, doi:10.5194/acp-10-7775-2010, 2010. 20379, 20380

Kaleschke, L., Richter, A., Burrows, J., Afe, O., Heygster, G., Notholt, J., Rankin, A. M., Roscoe, H. K., Hollwedel, J., Wagner, T., and Jacobi, H. W.: Frost flowers on sea ice as a source of sea salt and their influence on tropospheric halogen chemistry, Geophys. Res. Lett., 31, L16114, doi:10.1029/2004GL020655, 2004. 20344

Keene, W. C., Pszenny, A. A. P., Maben, J. R., and Sander, R.: Variation of marine aerosol acidity with particle size, Geophys. Res. Lett., 29, 5-1–5-4, doi:10.1029/2001GL013881, 2002. 20366

ACPD
13, 20341–20418, 2013

King, M. D. and Simpson, W. R.: Extinction of UV radiation in Arctic snow at Alert, Canada (82° N), J. Geophys. Res., 106, 12499–12507, 2001. 20350, 20351
Koop, T., Kapilashrami, A., Molina, L. T., and Molina, M. J.: Phase transitions of sea-salt/water mixtures at low temperatures: Implications for ozone chemistry in the polar marine boundary layer, J. Geophys. Res., 105, 26393–26402, 2000. 20353, 20365
Kuo, M. H., Moussa, S. G., and McNeill, V. F.: Modeling interfacial liquid layers on environmental ices, Atmos. Chem. Phys., 11, 9971–9982, doi:10.5194/acp-11-9971-2011, 2011. 20367
Kylling, A., Stamnes, K., and Tsay, S.-C.: A reliable and efficient two-stream algorithm for spherical radiative transfer: documentation of accuracy in realistic layered media, J. Atmos. Chem., 21, 115–150, 1995. 20350
Laird, S. K., Buttry, D. A., and Sommerfeld, R. A.: Nitric acid adsorption on ice: surface diffusion, Geophys. Res. Lett., 26, 699–701, 1999. 20354
Lehrer, E., Hönninger, G., and Platt, U.: A one dimensional model study of the mechanism of halogen liberation and vertical transport in the polar troposphere, Atmos. Chem. Phys., 4, 2427–2440, doi:10.5194/acp-4-2427-2004, 2004. 20345, 20372, 20374
Li, S.-M.: Equilibrium of particle nitrite with gas-phase HONO: tropospheric measurements in the high arctic during polar sunrise, J. Geophys. Res., 99, 25469–25478, 1994. 20361
Liao, J., Sihler, H., Huey, L. G., Neuman, J. A., Tanner, D. J., Friess, U., Platt, U., Flocke, F. M., Orlando, J. J., Shepson, P. B., Beine, H. J., Weinheimer, A. J., Sjostedt, S. J., Nowak, J. B., Knapp, D. J., Staebler, R. M., Zheng, W., Sander, R., Hall, S. R., and Ullmann, K.: A comparison of Arctic BrO measurements by chemical ionization mass spectrometry and long path differential optical absorption spectroscopy, J. Geophys. Res., 116, D00R02, doi:10.1029/2010JD014788, 2011. 20372
Mahajan, A. S., Shaw, M., Oetjen, H., Hornsby, K. E., Carpenter, L. J., Kaleschke, L., Tian-Kunze, X., Lee, J. D., Moller, S. J., Edwards, P., Commane, R., Ingham, T., Heard, D. E., and Plane, J. M. C.: Evidence of reactive iodine chemistry in the Arctic boundary layer, J. Geophys. Res., 115, D20303, doi:10.1029/2009JD013665, 2010. 20344
Mahrt, L.: The near-calm stable boundary layer, Bound.-Lay. Meteorol., 140, 343–360, 2011. 20359
Marion, G. M. and Farren, R. E.: Mineral solubilities in the Na-K-Mg-Ca-Cl-SO_4-H_2O system: a re-evaluation of the sulfate chemistry in the Spencer–Møller–Weare model, Geochim. Cosmochim. Ac., 63, 1305–1318, 1999. 20367

ACPD
13, 20341–20418, 2013

Massom, R. A., Lytle, V. I., Worby, A. P., and Allison, I.: Winter snow cover variability on East Antarctic sea ice, J. Geophys. Res., 103, 24837–24855, 1998. 20365, 20382

Matthew, B. M., George, I., and Anastasio, C.: Hydroperoxyl radical ($HO_2\cdot$) oxidizes dibromide radical anion ($\cdot Br_2^-$) to bromine (Br_2) in aqueous solution: implications for the formation of Br_2 in the marine boundary layer, Geophys. Res. Lett., 30, 2297, doi:10.1029/2003GL018572, 2003. 20349

McConnell, J. C., Henderson, G. S., Barrie, L., Bottenheim, J., Niki, H., Langford, C. H., and Templeton, E. M. J.: Photochemical bromine production implicated in Arctic boundary-layer ozone depletion, Nature, 355, 150–152, 1992. 20344

McElroy, C. T., McLinden, C. A., and McConnell, J. C.: Evidence for bromine monoxide in the free troposphere during the Arctic polar sunrise, Nature, 397, 338–341, 1999. 20379

Michalowski, B. A., Francisco, J. S., Li, S. M., Barrie, L. A., Bottenheim, J. W., and Shepson, P. B.: A computer model study of multiphase chemistry in the Arctic boundary layer during polar sunrise, J. Geophys. Res., 105, 15131–15145, 2000. 20344, 20345, 20348, 20374

Millero, F. J., Feistel, R., Wright, D. G., and McDougall, T. J.: The composition of standard seawater and the definition of the reference-composition salinity scale, Deep-Sea Res. I, 55, 50–72, 2008. 20404

Morin, S., Hönninger, G., Staebler, R. M., and Bottenheim, J. W.: A high time resolution study of boundary layer ozone chemistry and dynamics over the Arctic Ocean near Alert, Nunavut, Geophys. Res. Lett., 32, L08809, doi:10.1029/2004GL022098, 2005. 20344

Muller, J. B., Dorsey, J. R., Flynn, M., Gallagher, M. W., amd Dudley E. Shallcross, C. J. P., Archibald, A., Roscoe, H. K., Obbard, R. W., Atkinson, H. M., Lee, J. D., Moller, S. J., and Carpenter, L. J.: Energy and ozone fluxes over sea ice, Atmos. Environ., 47, 218–225, 2012. 20378, 20381

Murphy, D. M. and Koop, T.: Review of the vapour pressures of ice and supercooled water for atmospheric applications, Q. J. R. Meteorol. Soc., 131, 1539–1565, doi:10.1256/qj.04.94, 2005. 20361

Obbard, R. W., Roscoe, H. K., Wolff, E. W., and Atkinson, H. M.: Frost flower surface area and chemistry as a function of salinity and temperature, J. Geophys. Res., 114, D20305, doi:10.1029/2009JD012481, 2009. 20365

ACPD
13, 20341–20418, 2013

Oldridge, N. W. and Abbatt, J. P. D.: Formation of gas-phase bromine from interaction of ozone with frozen and liquid NaCl/NaBr solutions: quantitative separation of surficial chemistry from bulk-phase reaction, J. Phys. Chem. A, 115, 2590–2598, 2011. 20344, 20373

Oltmans, S. J.: Surface ozone measurements in clean air, J. Geophys. Res., 86, 1174–1180, 1981. 20343

Persson, P. O. G., Fairall, C. W., Andreas, E. L., Guest, P. S., and Perovich, D. K.: Measurements near the atmospheric surface flux group tower at SHEBA: near-surface conditions and surface energy budget, J. Geophys. Res., 107, 8045, doi:10.1029/2000JC000705, 2002. 20357, 20403

Peterson, M. and Honrath, R.: Observations of rapid photochemical destruction of ozone in snowpack interstitial air, Geophys. Res. Lett., 28, 511–514, 2001. 20375

Peterson, M., Barber, D., and Green, S.: Monte Carlo modeling and measurements of actinic flux levels in Summit, Greenland snowpack, Atmos. Environ., 36, 2545–2551, 2002. 20350

Petroff, A. and Zhang, L.: Development and validation of a size-resolved particle dry deposition scheme for application in aerosol transport models, Geosci. Model Dev., 3, 753–769, doi:10.5194/gmd-3-753-2010, 2010. 20361, 20362

Piot, M. and von Glasow, R.: The potential importance of frost flowers, recycling on snow, and open leads for ozone depletion events, Atmos. Chem. Phys., 8, 2437–2467, doi:10.5194/acp-8-2437-2008, 2008. 20344, 20365, 20376

Pisso, I., Real, E., Law, K. S., Legras, B., Bousserez, N., Attié, J. L., and Schlager, H.: Estimation of mixing in the troposphere from Lagrangian trace gas reconstructions during long-range pollution plume transport, J. Geophys. Res., 114, D19301, doi:10.1029/2008JD011289, 2009. 20360

Platt, U. and Lehrer, E.: Arctic Tropospheric Ozone Chemistry, ARCTOC, Final Report of the EU-Project No. EV5V-CT93-0318, Heidelberg, 1996. 20344

Pöhler, D., Vogel, L., Frieß, U., and Platt, U.: Observation of halogen species in the Amundsen Gulf, Arctic, by active long-path differential optical absorption spectroscopy, P. Natl. Acad. Sci., 107, 6582–6587, doi:10.1073/pnas.0912231107, 2010. 20344, 20364, 20372

Pratt, K. A., Custard, K. D., Shepson, P. B., Douglas, T. A., Pöhler, D., General, S., Zielcke, J., Simpson, W. R., Platt, U., Tanner, D. J., Gregory Huey, L., Carlsen, M., and Stirm, B. H.: Photochemical production of molecular bromine in Arctic surface snowpacks, Nature Geosci., 6, 351–356, doi:10.1038/ngeo1779, 2013. 20344, 20381

ACPD
13, 20341–20418, 2013

Press, W. H., Flannery, B. P., Teukolsky, S. A., and Vetterling, W. T.: Numerical Recipes in FORTRAN 77: the Art of Scientific Computing, 2nd edn., Cambridge Univ. Press, Cambridge, UK, 1992. 20363

Qiu, R., Green, S. A., Honrath, R. E., Peterson, M. C., Lu, Y., and Dziobak, M.: Measurements of $J_{NO_3^-}$ in snow by nitrate-based actinometry, Atmos. Environ., 36, 2563–2571, 2002. 20350

Quinn, P. K., Shaw, G., Andrews, E., Dutton, E. G., Ruoho-Airola, T., and Gong, S. L.: Arctic haze: current trends and knowledge gaps, Tellus B, 59, 99–114, 2007. 20360

Ramacher, B., Rudolph, J., and Koppmann, R.: Hydrocarbon measurements during tropospheric ozone depletion events: evidence for halogen atom chemistry, J. Geophys. Res., 104, 3633–3653, 1999. 20373

Rankin, A. M., Wolff, E. W., and Martin, S.: Frost flowers: implications for tropospheric chemistry and ice core interpretation, J. Geophys. Res., 107, 4683, doi:10.1029/2002JD002492, 2002. 20344

Real, E., Pisso, I., Law, K. S., Legras, B., Bousserez, N., Schlager, H., Roiger, A., and Attié, J. L.: Toward a novel high-resolution modeling approach for the study of chemical evolution of pollutant plumes during long-range transport, J. Geophys. Res., 115, D12302, doi:10.1029/2009JD011707, 2010. 20360

Reay, H. J., France, J. L., and King, M. D.: Decreased albedo, e-folding depth and photolytic OH radical and NO_2 production with increasing black carbon content in Arctic snow, J. Geophys. Res., 117, D00R20, doi:10.1029/2011JD016630, 2012. 20350

Richter, A., Wittrock, F., Eisinger, M., and Burrows, J. P.: GOME observations of tropospheric BrO in northern hemispheric spring and summer 1997, Geophys. Res. Lett., 25, 2683–2686, 1998. 20378

Saiz-Lopez, A., Mahajan, A. S., Salmon, R. A., Bauguitte, S. J.-B., Jones, A. E., Roscoe, H. K., and Plane, J. M. C.: Boundary layer halogens in coastal Antarctica, Science, 317, 348–351, 2007. 20344

Saiz-Lopez, A., Plane, J. M. C., Mahajan, A. S., Anderson, P. S., Bauguitte, S. J.-B., Jones, A. E., Roscoe, H. K., Salmon, R. A., Bloss, W. J., Lee, J. D., and Heard, D. E.: On the vertical distribution of boundary layer halogens over coastal Antarctica: implications for O_3, HO_x, NO_x and the Hg lifetime, Atmos. Chem. Phys., 8, 887–900, doi:10.5194/acp-8-887-2008, 2008. 20344

Salawitch, R. J., Canty, T., Kurosu, T., Chance, K., Liang, Q., da Silva, A., Pawson, S., Nielsen, J. E., Rodriguez, J., Bhartia, P., Liu, X., Huey, L., Liao, J., Stickel, R., Simpson, W.,

ACPD
13, 20341–20418, 2013

Donohoue, D., Weinheimer, A., Flocke, F., Knapp, D., Montzka, D., Neuman, J., Nowak, J., Ryerson, T., Oltmans, S., Blake, D., Atlas, E. L., Kinnison, D., Tilmes, S., Pan, L., Hendrick, F., Roozendael, M. V., Kreher, K., Johnston, P., Gao, R. S., Johnson, B., Bui, T., Chen, G., Pierce, R. B., Crawford, J. H., and Jacob, D. J.: A new interpretation of total column BrO during Arctic Spring, Geophys. Res. Lett., 37, L21805, doi:10.1029/2010GL043798, 2010. 20379

Sander, R. and Bottenheim, J.: A compilation of tropospheric measurements of gas-phase and aerosol chemistry in polar regions, Earth Syst. Sci. Data, 4, 215–282, doi:10.5194/essd-4-215-2012, 2012. 20367, 20405

Sander, R., Vogt, R., Harris, G. W., and Crutzen, P. J.: Modeling the chemistry of ozone, halogen compounds, and hydrocarbons in the arctic troposphere during spring, Tellus B, 49, 522–532, 1997. 20343, 20369

Sander, R., Burrows, J., and Kaleschke, L.: Carbonate precipitation in brine – a potential trigger for tropospheric ozone depletion events, Atmos. Chem. Phys., 6, 4653–4658, doi:10.5194/acp-6-4653-2006, 2006. 20349

Schroeder, W. H., Anlauf, K. G., Barrie, L. A., Lu, J. Y., Steffen, A., R.Schneeberger, D., and Berg, T.: Arctic springtime depletion of mercury, Nature, 394, 331–332, 1998. 20343

Schumann, U., Konopka, P., Baumann, R., Busen, R., Gertz, T., Schlager, H., Schulte, P., and Volkert, H.: Estimate of diffusion parameters of aircraft exhaust plumes near the tropopause from nitric oxide ond turbulence measurements, J. Geophys. Res., 100, 14147–14162, 1995. 20360

Schwartz, S. E.: Mass-transport considerations pertinent to aqueous phase reactions of gases in liquid-water clouds, in: Chemistry of Multiphase Atmospheric Systems, edited by: Jaeschke, W., Springer-Verlag, New York, 415–471, 1986. 20348

Seabrook, J. A., Whiteway, J., Staebler, R. M., Bottenheim, J. W., Komguem, L., Gray, L. H., Barber, D., and Asplin, M.: LIDAR measurements of Arctic boundary layer ozone depletion events over the frozen Arctic Ocean, J. Geophys. Res., 116, D00S02, doi:10.1029/2011JD016335, 2011. 20344

Seabrook, J. A., Whiteway, J. A., Gray, L. H., Staebler, R., and Herber, A.: Airborne lidar measurements of surface ozone depletion over Arctic sea ice, Atmos. Chem. Phys., 13, 6023–6029, doi:10.5194/acp-13-6023-2013, 2013. 20344

Seinfeld, J. H. and Pandis, S. N.: Atmospheric Chemistry and Physics: From Air Pollution to Climate Change, J. Wiley, New York, 1998. 20402

ACPD
13, 20341–20418, 2013

Semb, A., Brækkan, R., and Joranger, E.: Major ions in Spitsbergen snow samples, Geophys. Res. Lett., 11, 445–448, 1984. 20366
Sihler, H., Platt, U., Beirle, S., Marbach, T., Kühl, S., Dörner, S., Verschaeve, J., Frieß, U., Pöhler, D., Vogel, L., Sander, R., and Wagner, T.: Tropospheric BrO column densities in the Arctic derived from satellite: retrieval and comparison to ground-based measurements, Atmos. Meas. Tech., 5, 2779–2807, doi:10.5194/amt-5-2779-2012, 2012. 20379
Simpson, W. R., King, M. D., Beine, H. J., Honrath, R. E., and Zhou, X.: Radiation-transfer modeling of snow-pack photochemical processes during ALERT 2000, Atmos. Environ., 36, 2663–2670, 2002. 20350
Simpson, W. R., Alvarez-Aviles, L., Douglas, T. A., Sturm, M., and Domine, F.: Halogens in the coastal snow pack near Barrow, Alaska: evidence for active bromine air–snow chemistry during springtime, Geophys. Res. Lett., 32, L04811, doi:10.1029/2004GL021748, 2005. 20344, 20365
Simpson, W. R., von Glasow, R., Riedel, K., Anderson, P., Ariya, P., Bottenheim, J., Burrows, J., Carpenter, L. J., Frieß, U., Goodsite, M. E., Heard, D., Hutterli, M., Jacobi, H.-W., Kaleschke, L., Neff, B., Plane, J., Platt, U., Richter, A., Roscoe, H., Sander, R., Shepson, P., Sodeau, J., Steffen, A., Wagner, T., and Wolff, E.: Halogens and their role in polar boundary-layer ozone depletion, Atmos. Chem. Phys., 7, 4375–4418, doi:10.5194/acp-7-4375-2007, 2007. 20343, 20344, 20345
Smith, R. S. and Kay, B. D.: The existence of supercooled liquid water at 150 K, Nature, 398, 788–791, 1999. 20354
Staebler, R. M., den Hartog, G., Giorgi, B., and Düsterdiek, T.: Aerosol size distributions in Arctic haze during the Polar Sunrise Experiment 1992, J. Geophys. Res., 99, 25429–25437, 1992. 20360
Staebler, R., Toom-Sauntry, D., Barrie, L., Langendörfer, U., Lehrer, E., Li, S.-M., and Dryfhout-Clark, H.: Physical and chemical characteristics of aerosols at Spitsbergen in the spring of 1996, J. Geophys. Res., 104, 5515–5529, 1999. 20361
Steeneveld, G. J., van de Wiel, B. J. H., and Holtslag, A. A. M.: Diagnostic equations for the stable boundary layer heights: evaluation and dimensional analysis, J. Appl. Meteorol. Clim., 46, 212–225, 2007. 20356, 20403
Steffen, A., Douglas, T., Amyot, M., Ariya, P., Aspmo, K., Berg, T., Bottenheim, J., Brooks, S., Cobbett, F., Dastoor, A., Dommergue, A., Ebinghaus, R., Ferrari, C., Gardfeldt, K., Goodsite, M. E., Lean, D., Poulain, A. J., Scherz, C., Skov, H., Sommar, J., and Temme, C.: A

ACPD
13, 20341–20418, 2013

synthesis of atmospheric mercury depletion event chemistry in the atmosphere and snow, Atmos. Chem. Phys., 8, 1445–1482, doi:10.5194/acp-8-1445-2008, 2008. 20343
Stokes, R. H. and Robinson, R. A.: Interactions in aqueous nonelectrolyte solutions, I. Solute-solvent equilibria, J. Phys. Chem., 70, 2126–2130, 1966. 20360
Sturm, M., Holmgren, J., and Perovich, D. K.: Winter snow cover on the sea ice of the Arctic Ocean at the Surface Heat Budget of the Arctic Ocean (SHEBA): temporal evolution and spatial variability, J. Geophys. Res., 107, 8047, doi:10.1029/2000JC000400, 2002. 20347, 20384
Tang, I. N.: Chemical and size effects of hygroscopic aerosols on light scattering coefficients, J. Geophys. Res., 101, 19245–19250, 1996. 20361
Tang, I. N.: Thermodynamic and optical properties of mixed-salt aerosols of atmospheric importance, J. Geophys. Res., 102, 1883–1893, 1997. 20361
Tang, I. N. and Munkelwitz, H. R.: Water activities, densities, and refractive indices of aqueous sulfates and sodium nitrate droplets of atmospheric importance, J. Geophys. Res., 99, 18801–18808, 1994. 20361
Tang, T. and McConnell, J. C.: Autocatalytic release of bromine from Arctic snow pack during polar sunrise, Geophys. Res. Lett., 23, 2633–2636, 1996. 20345, 20367, 20374
Tarasick, D. W. and Bottenheim, J. W.: Surface ozone depletion episodes in the Arctic and Antarctic from historical ozonesonde records, Atmos. Chem. Phys., 2, 197–205, doi:10.5194/acp-2-197-2002, 2002. 20364
Theys, N., Van Roozendael, M., Hendrick, F., Yang, X., De Smedt, I., Richter, A., Begoin, M., Errera, Q., Johnston, P. V., Kreher, K., and De Mazière, M.: Global observations of tropospheric BrO columns using GOME-2 satellite data, Atmos. Chem. Phys., 11, 1791–1811, doi:10.5194/acp-11-1791-2011, 2011. 20379
Thomas, J. L., Stutz, J., Lefer, B., Huey, L. G., Toyota, K., Dibb, J. E., and von Glasow, R.: Modeling chemistry in and above snow at Summit, Greenland – Part 1: Model description and results, Atmos. Chem. Phys., 11, 4899–4914, doi:10.5194/acp-11-4899-2011, 2011. 20346, 20351, 20353, 20373, 20375, 20376
Toom-Sauntry, D. and Barrie, L. A.: Chemical composition of snowfall in the high Arctic: 1990–1994, Atmos. Environ., 36, 2683–2693, 2002. 20366
Toyota, K., Kanaya, Y., Takahashi, M., and Akimoto, H.: A box model study on photochemical interactions between VOCs and reactive halogen species in the marine boundary layer, Atmos. Chem. Phys., 4, 1961–1987, doi:10.5194/acp-4-1961-2004, 2004. 20349, 20369

ACPD
13, 20341–20418, 2013

Toyota, K., McConnell, J. C., Lupu, A., Neary, L., McLinden, C. A., Richter, A., Kwok, R., Semeniuk, K., Kaminski, J. W., Gong, S.-L., Jarosz, J., Chipperfield, M. P., and Sioris, C. E.: Analysis of reactive bromine production and ozone depletion in the Arctic boundary layer using 3-D simulations with GEM-AQ: inference from synoptic-scale patterns, Atmos. Chem. Phys., 11, 3949–3979, doi:10.5194/acp-11-3949-2011, 2011. 20344, 20364, 20382

Toyota, K., Dastoor, A. P., and Ryzhkov, A.: Air-snowpack exchange of bromine, ozone and mercury in the springtime Arctic simulated by the 1-D model PHANTAS – Part 2: Mercury and its speciation, Atmos. Chem. Phys. Discuss., submitted, 2013. 20346, 20349, 20351, 20360, 20367

Tuckermann, M., Ackermann, R., Göltz, C., Lorenzen-Schmidt, H., Senne, T., Stutz, J., Trost, B., Unold, W., and Platt, U.: DOAS-observation of halogen radical-catalysed arctic boundary layer ozone destruction during the ARCTOC-campaigns 1995 and 1996 in Ny-Ålesund, Spitsbergen, Tellus B, 49, 533–555, 1997. 20344

Voss, L. F., Henson, B. F., Wilson, K. R., and Robinson, J. M.: Atmospheric impact of quasiliquid layers on ice surfaces, Geophys. Res. Lett., 32, L07807, doi:10.1029/2004GL022010, 2005. 20353

Wagner, T. and Platt, U.: Satellite mapping of enhanced BrO concentrations in the troposphere, Nature, 395, 486–490, 1998. 20378

Warren, S. G. and Wiscombe, W. J.: A model for the spectral albedo of snow, II: snow containing atmospheric aerosols, J. Atmos. Sci., 37, 2734–2745, 1980. 20350

Warren, S. G., Rigor, I. G., Untersteiner, N., Radionov, V. F., Bryazgin, N. N., Aleksandrov, Y. I., and Colony, R.: Snow depth on Arctic sea ice, J. Climate, 12, 1814–1829, 1999. 20347, 20384

Weeks, W. F. and Hibler III, W. D.: On Sea Ice, Univ. Alaska Press, Fairbanks, Alaska, 2000. 20366

Wennberg, P.: Bromine explosion, Nature, 397, 299–301, 1999. 20344

Wesely, M. L.: Parameterization of surface resistances to gaseous dry deposition in regional-scale numerical models, Atmos. Environ., 23, 1293–1304, 1989. 20376

Wessel, S., Aoki, S., Winkler, P., Weller, R., Herber, A., Gernandt, H., and Schrems, O.: Tropospheric ozone depletion in polar regions, a comparison of observations in the Arctic and Antarctic, Tellus B, 50, 34–50, 1998. 20343

Wolff, E. W. and Paren, J. G.: A two-phase model of electrical conduction in polar ice sheets, J. Geophys. Res., 89, 9433–9438, 1984. 20354

ACPD
13, 20341–20418, 2013

Wren, S. N., Donaldson, D. J., and Abbatt, J. P. D.: Photochemical chlorine and bromine activation from artificial saline snow, Atmos. Chem. Phys. Discuss., 13, 14163–14193, doi:10.5194/acpd-13-14163-2013, 2013. 20381

Yang, X., Pyle, J. A., and Cox, R. A.: Sea salt aerosol production and bromine release: role of snow on sea ice, Geophys. Res. Lett., 35, L16815, doi:10.1029/2008GL034536, 2008. 20344, 20345, 20360, 20382, 20383

Zdanovskii, A. B.: New methods for calculating solubilities of electrolytes in multicomponent systems, Zhur. Fiz. Khim., 22, 1475–1485, 1948. 20360

Zilitinkevich, S. S. and Esau, I. N.: The effect of baroclinicity on the equilibrium depth of neutral and stable planetary boundary layers, Q. J. R. Meteorol. Soc., 129, 3339–3356, doi:10.1256/qj.02.94, 2003. 20356

ACPD
13, 20341–20418, 2013

Table 1. Parameterizations used for the vertical diffusivity of gaseous and aqueous-phase (atmospheric aerosols and snowpack LLL) composition in different model domains.

	Snowpack	Atmosphere	
		$z < Z_{ABL}$	$z \geq Z^{a}_{ABL}$
Gas-phase species, $D_{g,z}$	D_{SIA}, Eq. (5)	$K(z)$, Eq. (10)	$D^{b}_{g,mol}$
Aqueous-phase species, $D_{a,z}$	D_{LLL}, Eq. (9)	$K(z)$, Eq. (10)	D^{c}_{B}

[a] Z_{ABL} is the depth of the turbulent ABL calculated diagnostically by Eq. (14).
[b] $D_{g,mol}$ is the molecular diffusivity of gaseous molecules in air and calculated according to Fuller et al. (1966, 1969).
[c] D_B is the Brownian diffusivity of aerosols in air and calculated according to Seinfeld and Pandis (1998).

ACPD
13, 20341–20418, 2013

Table 2. Summary of meteorological and geographic conditions used in the model runs.

Parameter	Values	Reference
Latitude	71° N	
Date	30 March	
Total column ozone	400 Dobson unit	
Temperature	253 K	
Pressure	1013.25 hPa	
Relative humidity with respect to ice	98 %[a]	Andreas et al. (2002)
Reference-height wind speed (U_2)	2, 4.5, 8.5 or 12 m s^{-1}	
Sensible heat flux at the bottom of the atmosphere (F_{SH})	-5 ± 4 W m^{-2}[b]	Persson et al. (2002)
Brunt–Väisälä frequency in the free atmosphere (N)	0.031 s^{-1}[c]	Steeneveld et al. (2007)

[a] At T = 253 K and p = 1013.25 hPa, it is equivalent to relative humidity with respect to water at 80.46 % (see Sect. 2.8).
[b] A sinusoidal function to represent diurnal variations is assigned by the present authors (see Eq. (19) in Sect. 2.7).
[c] In Sect. 3.4, sensitivity runs are also performed by using the high- and low-ends (0.046 s^{-1} and 0.016 s^{-1}, respectively) of the N values inferred by Steeneveld et al. (2007).

ACPD
13, 20341–20418, 2013

Table 3. Initial conditions for condensed-phase chemistry in the snowpack.

Parameter	Initial value	Reference
Bulk concentration of Cl^-	70 µmol L^{-1}	Cho et al. (2002)
Bulk concentration of Br^-	0.108 µmol L^{-1} (= 1/650 × $[Cl^-]$)	Millero et al. (2008)
Bulk concentration of NO_3^-	2 µmol L^{-1}	Grannas et al. (2007)
Bulk concentration of HCO_3^- (alkalinity)	0[a]	
Bulk concentration of Na^+	72 µmol L^{-1}	
pH in LLL	4	
Volume fraction of LLL (f_q)	1.11×10^{-5}[b]	

[a] Assumed to have been titrated by the atmospheric input of NO_3^- (see text).

[b] Calculated according to Cho et al. (2002) based on the sum of dissolved ion concentrations in the LLL (see Sect. 2.5).

ACPD
13, 20341–20418, 2013

Table 4. Initial and upper boundary conditions for key trace gases (in both the atmosphere and the SIA) and aerosol composition.

Gas-phase species[a]	
Species	Mixing ratio
O_3	40 nmol mol^{-1}
H_2O_2	250 pmol mol^{-1}
NO_2	15 pmol mol^{-1}
HNO_3	100 pmol mol^{-1}
PAN	200 pmol mol^{-1}
CH_4	1.85 µmol mol^{-1}
C_2H_6	1.7 nmol mol^{-1}
C_2H_2	400 pmol mol^{-1}
CO	150 nmol mol^{-1}
HCHO	150 pmol mol^{-1}[b]
CH_3CHO	50 pmol mol^{-1}[b]
CH_3OOH	250 pmol mol^{-1}
$CHBr_3$	3.5 pmol mol^{-1} (fixed)
HCl	100 pmol mol^{-1}
SO_2	100 pmol mol^{-1}
CO_2	380 µmol mol^{-1}
Aerosol composition[c]	
Species	Concentration
$HSO_4^- + SO_4^{2-}$	12 nmol m^{-3}(STP)
NH_4^+	9.6 nmol m^{-3}(STP)
Cl^-	0
Br^-	0
pH	~ −0.09

[a] Initial mixing ratios for gas-phase species are selected on the basis of observational data compilations (Evans et al., 2003; Sander and Bottenheim, 2012, and references therein).
[b] To start model runs with the concentrations of HCHO and CH_3CHO closer to their near-steady state conditions constrained strongly by in-snow emissions, their initial concentrations in the SIA are raised by a factor of 2. Furthermore, the initial concentrations of their dissolved forms (including hydrate) in the LLL are set in thermodynamic equilibria with the concentrations of respective gases in the SIA.
[c] See Sect. 2.8 for details on initial sulfate and ammonium concentrations and aerosol pH.

ACPD
13, 20341–20418, 2013

Table 5. In-snow emissions for HCHO and CH_3CHO.

Species	Emission rate[a]	Reference
HCHO	4.8×10^8 molecule cm^{-2} s^{-1}	Grannas et al. (2002)
CH_3CHO	4.25×10^8 molecule cm^{-2} s^{-1}	Guimbaud et al. (2002)

[a] Vertically integrated and diurnal averaged in-snow emission rates are given here. During model runs, the emission rates are scaled in time and in space according to J values for $O_3 + h\nu \rightarrow O(^1D) + O_2$.

ACPD
13, 20341–20418, 2013

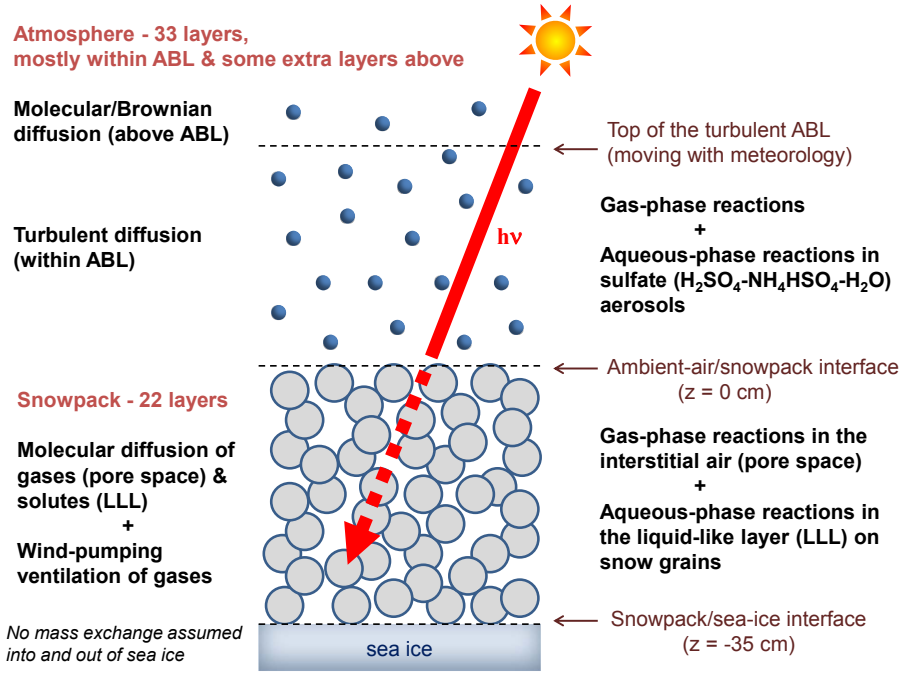

Fig. 1. Vertical domains and physical/chemical processes represented by PHANTAS.

ACPD
13, 20341–20418, 2013

Air-snowpack exchange of bromine and ozone

K. Toyota et al.

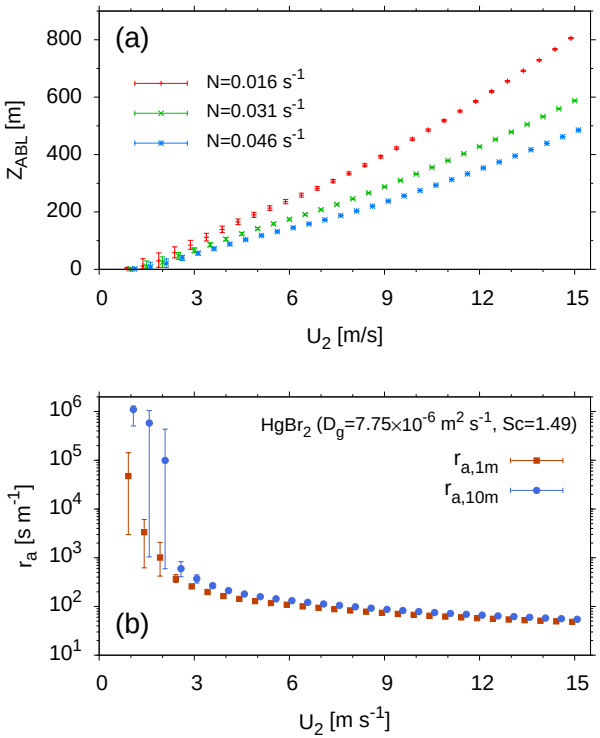

Fig. 2. (a) Changes in the diagnosed height of the turbulent atmospheric boundary layer (Z_{ABL}) with surface wind speeds (U_2) between 1∼15 m s^{-1} and Brunt–Väisälä frequencies in the free troposphere (N) between 0.016 ∼ 0.046 s^{-1}. Cross marks denote daily mean values while bars indicate the range of diurnal variations; **(b)** aerodynamic resistance for $HgBr_2$ from the snow surface to the height of either 1 m or 10 m in ambient air for U_2 = 1∼15 m s^{-1} at N = 0.031 s^{-1} as calculated in the present model. Filled squares and circles denote daily mean values while bars indicate the range of diurnal variations.

ACPD
13, 20341–20418, 2013

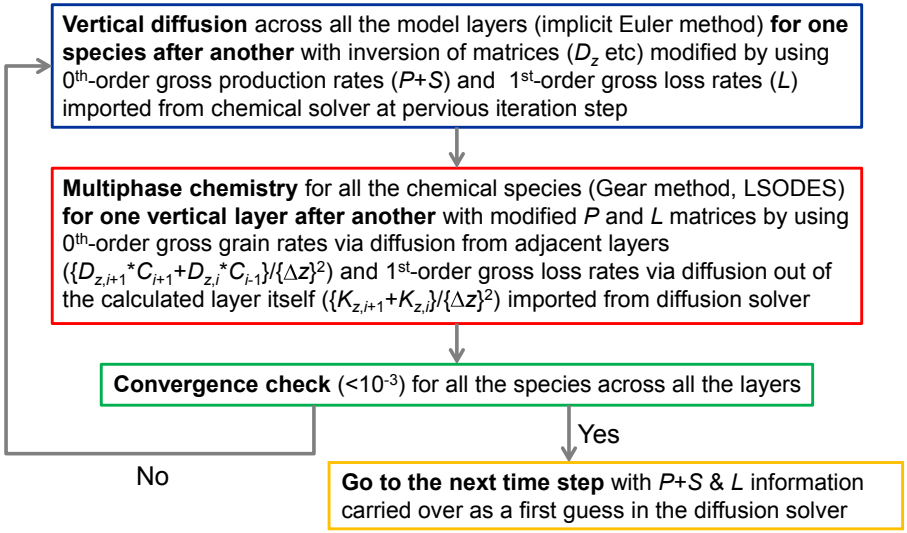

Fig. 3. The overview of a linearly coupled operator splitting with iteration between chemistry and diffusion solvers. C: tracer concentrations, P: chemical production rates, L: chemical loss rate constants, S: (parameterized) emission rates, and D_z: vertical diffusivity.

ACPD
13, 20341–20418, 2013

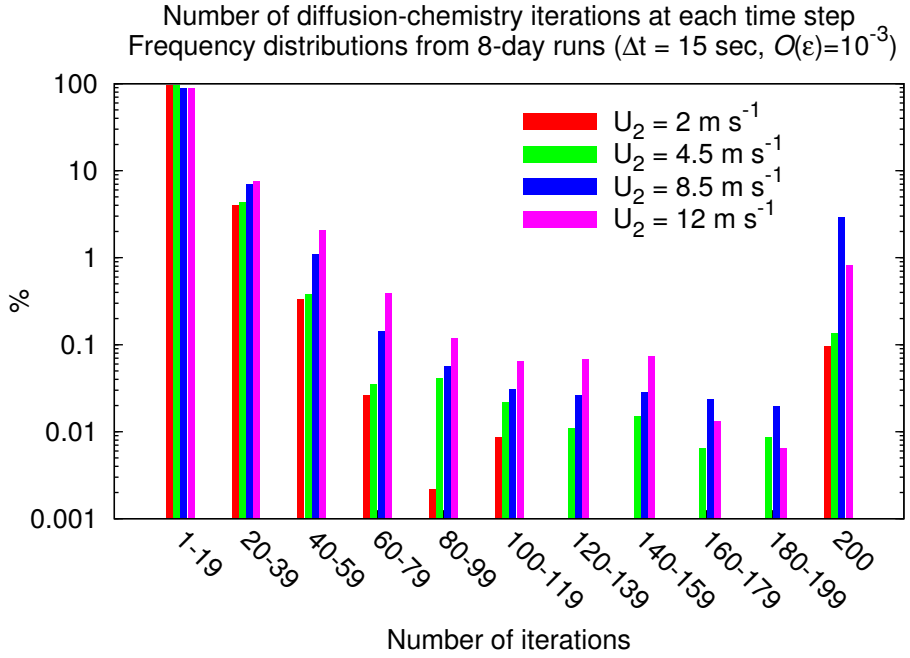

Fig. 4. Frequency distributions (over 8 model days) of iteration times spent by our numerical scheme with linearly coupled iteration between diffusion and chemistry solvers at each time step in model runs with $U_2 = 2\,\mathrm{m\,s^{-1}}$, $4.5\,\mathrm{m\,s^{-1}}$, $8.5\,\mathrm{m\,s^{-1}}$, and $12\,\mathrm{m\,s^{-1}}$. $N = 0.031\,\mathrm{s^{-1}}$ for all the model runs.

ACPD
13, 20341–20418, 2013

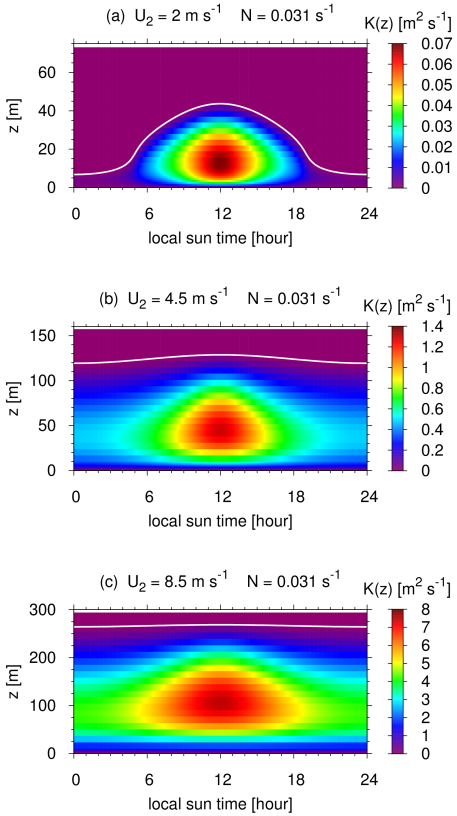

Fig. 5. Profiles and their diurnal variations of vertical diffusivity in the atmosphere prescribed by assuming $N = 0.031\,s^{-1}$ and $U_2 = 2\,m\,s^{-1}$ **(a)**, $4.5\,m\,s^{-1}$ **(b)** and $8.5\,m\,s^{-1}$ **(c)**. The white line in each graph indicates the level of Z_{ABL}, above which the vertical diffusion is assumed to be controlled by molecular diffusion for gases or by Brownian diffusion for aerosols.

ACPD
13, 20341–20418, 2013

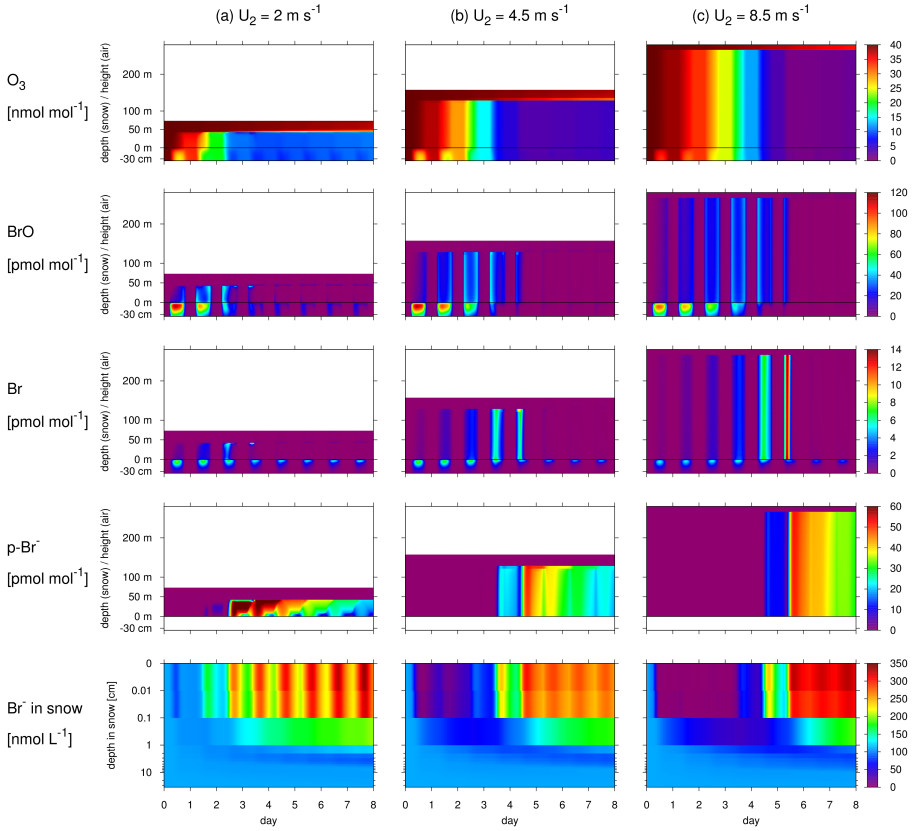

Fig. 6. Time-height cross sections for the mixing ratios of O_3 (top row), BrO (second row), Br-atom (third row), and aerosol bromide ($p\text{-}Br^-$, fourth row), and for the bulk concentrations of bromide in snowpack grains (bottom row) from model runs with $U_2 = 2\,m\,s^{-1}$ **(a)**, $4.5\,m\,s^{-1}$ **(b)**, and $8.5\,m\,s^{-1}$ **(c)**. $N = 0.031\,s^{-1}$ for all the model runs.

ACPD
13, 20341–20418, 2013

Air-snowpack exchange of bromine and ozone

K. Toyota et al.

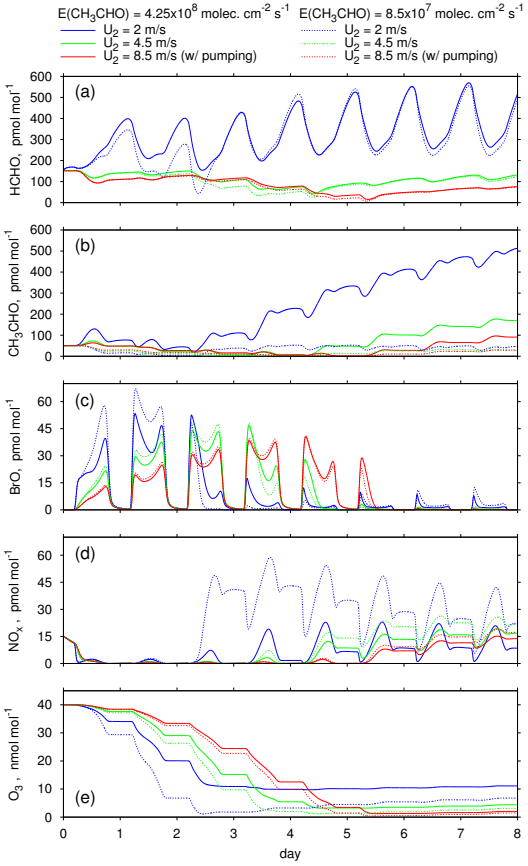

Fig. 7. Simulated mixing ratios of **(a)** HCHO, **(b)** CH_3CHO, **(c)** BrO, **(d)** NO_x (= NO + NO_2), and **(e)** O_3 at z = 1.5 m (ambient air) from model runs with snowpack emissions of CH_3CHO at "standard" (solid lines) and "low" (dotted lines) rates and with U_2 assigned at either 2 m s^{-1} (blue), 4.5 m s^{-1} (green), or 8.5 m s^{-1} (red).

ACPD
13, 20341–20418, 2013

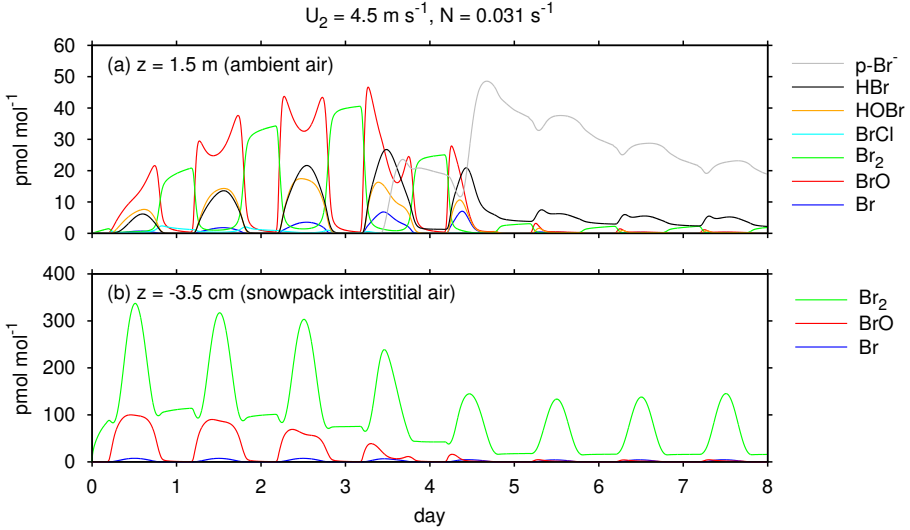

Fig. 8. Temporal evolutions of major bromine species at the height of **(a)** $z = 1.5\,\mathrm{m}$ (ambient air) and **(b)** $z = -3.5\,\mathrm{cm}$ (snowpack interstitial air) from a model run with $U_2 = 4.5\,\mathrm{m\,s^{-1}}$ and $N = 0.031\,\mathrm{s^{-1}}$.

ACPD
13, 20341–20418, 2013

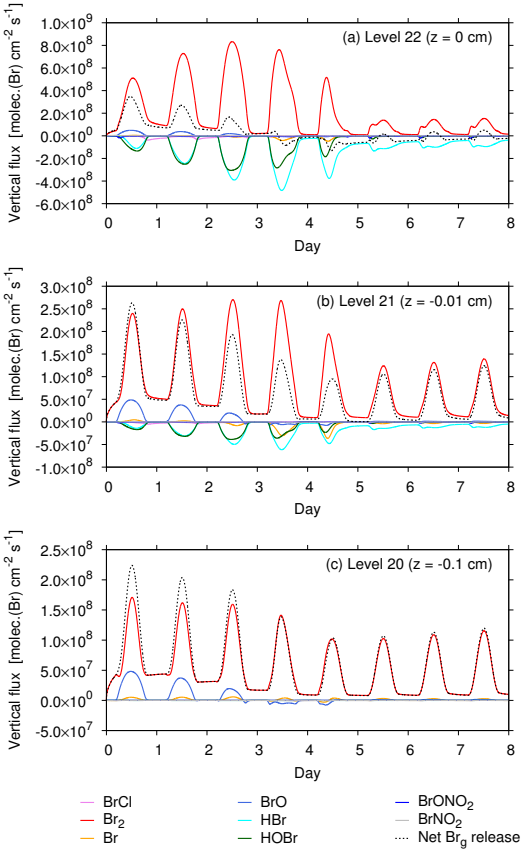

Fig. 9. Vertical fluxes of major inorganic bromine species in the top 1 mm of the snowpack as simulated at $U_2 = 4.5\,\mathrm{m\,s^{-1}}$ and $N = 0.031\,\mathrm{s^{-1}}$: **(a)** $z = 0$ cm (the top of the snowpack), **(b)** $z = -0.01$ cm, and **(c)** $z = -0.1$ cm.

ACPD
13, 20341–20418, 2013

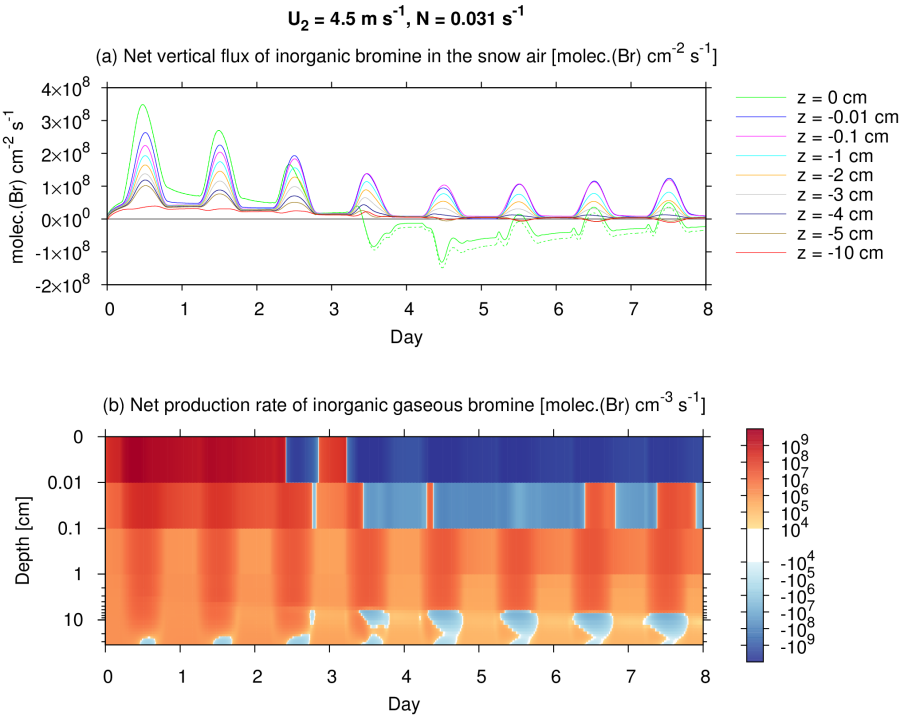

Fig. 10. Budget analyses of inorganic gaseous bromine in the snowpack as simulated in the model run with $U_2 = 4.5\,\mathrm{m\,s^{-1}}$ and $N = 0.031\,\mathrm{s^{-1}}$: **(a)** vertical fluxes at selected depth levels (solid lines) and the sum of the vertical fluxes of inorganic gaseous bromine and aerosol bromide at the top of the snowpack (green dotted line), and **(b)** net production (mostly via condensed-phase chemistry on the snow grain surface and subsequent release of products to the interstitial air).

ACPD
13, 20341–20418, 2013

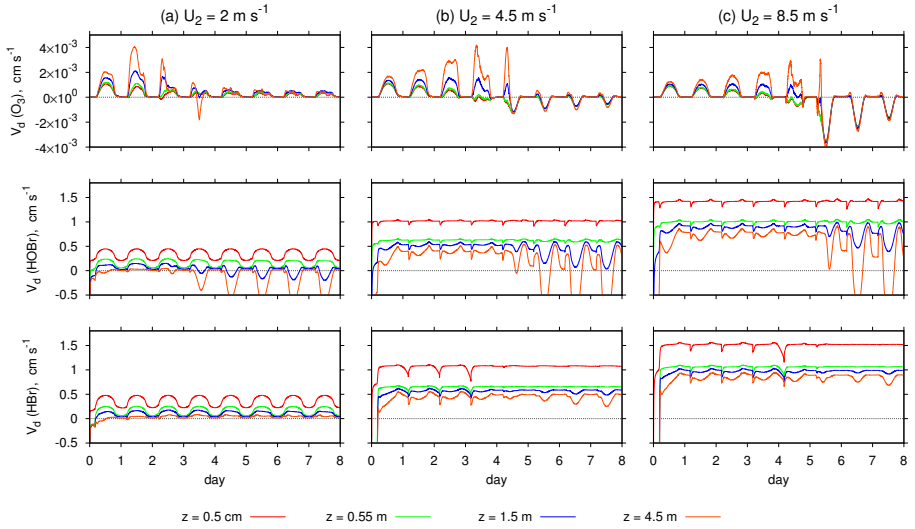

Fig. 11. Apparent dry deposition velocities (at 0.5 cm, 55 cm, 1.5 m, and 4.5 m above the snow surface) of O_3 (top row), HOBr (middle row) and HBr (bottom row) from model runs with $U_2 = 2.0\,m\,s^{-1}$ **(a)**, $4.5\,m\,s^{-1}$ **(b)** and $8.5\,m\,s^{-1}$ **(c)**.

ACPD
13, 20341–20418, 2013

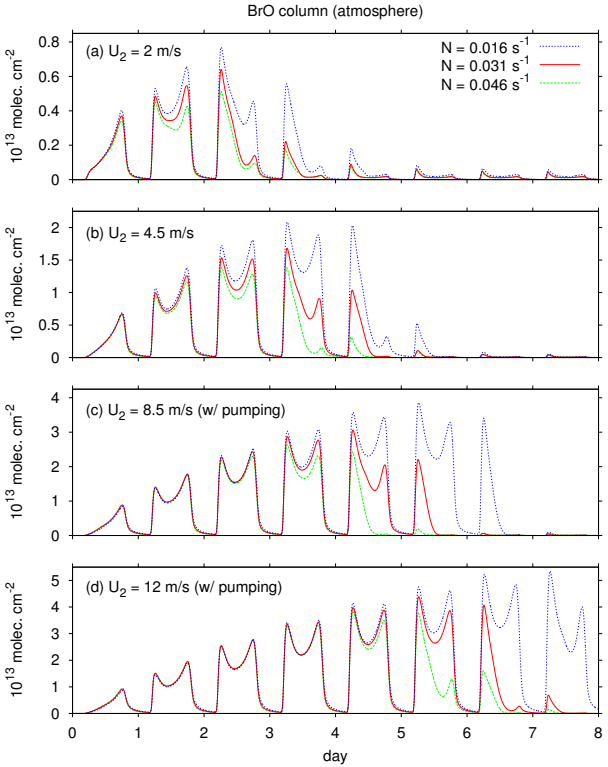

Fig. 12. Simulated column amounts of BrO in the atmosphere with U_2 assigned at **(a)** $2\,m\,s^{-1}$, **(b)** $4.5\,m\,s^{-1}$, **(c)** $8.5\,m\,s^{-1}$, and **(d)** $12\,m\,s^{-1}$. A sensitivity of the simulated BrO columns to the choice of N ($0.016\,s^{-1}$, dotted blue lines; $0.031\,s^{-1}$, solid red lines; and $0.046\,s^{-1}$, broken green lines) is also tested.

ACPD
13, 20341–20418, 2013